ISSN 1349-1113
JAXA-RR-04-046E

JAXA Research and Development Report

Lunar Imaging Camera (LIC) - Pre-flight tests and operation plan

March 2005

Japan Aerospace Exploration Agency

This document is provided by JAXA.

CONTENTS

This document is provided by JAXA.

This document is provided by JAXA.

Lunar Imaging Camera (LIC) - Pre-flight tests and operation plan

By

Akiko M. NAKAMURA[a)], Hiroaki SHIRAISHI[b)], Rie HONDA[c)], Yu-ichi IIJIMA[b)], Tatsuaki HASHIMOTO[b)], Keiken NINOMIYA[b*)], Yasuhiro YOKOTA[b)], Motomaro SHIRAO[d)], Toshiko TAKATA[e)], Atsushi YAMAJI[f)], Sho SASAKI[g)], Tatsuaki OKADA[b)], Tsuneo MATSUNAGA[h)], Hirohide DEMURA[i)], Naru HIRATA[a)], Chikatoshi HONDA[b)], Jun'ichi HARUYAMA[b)], Makiko OHTAKE[b)], Hirotomo NODA[g)], Hideaki MIYAMOTO[j)], Makoto YOSHIKAWA[b)], Satoshi TSUCHIDA[k)], Toshiki OHTAKI[k)], Hideki MURAKAMI[c)], Chosei KOMORI[d)]

And

Phillippe MASSON[l)], Patrick PINET[m)], Serge D. CHEVREL[m)], Yves DAYDOU[m)]

And

Masaru HIRAMATSU[n)]

Abstract : Lunar Imaging Camera (LIC) is a small, compact and lightweight monochromatic imager designed and developed for LUNAR-A, Japanese lunar mission. The scientific objectives of the camera address impact cratering, tectonic processes, volcanic features, and optical properties of the regolith surface.The image sensor is a linear CCD and is aligned with the spin axis of the spacecraft, which orbits the Moon at altitudes of 200-300 km. The two-dimensional image is taken using the spin motion of the spacecraft. The total field of view (FOV) of the camera is 360° (around the spin axis)×14.6° (along the CCD-array). LIC obtains an image in one spin. The angular resolution of the camera is about 20 arcsec/pixel at a spin rate of 3 rpm. The spatial resolution is about 25 m/pixels at the surface when the altitude is 250 km. The spin axis of the LUNAR-A approximately points toward the Sun, therefore, LIC can take images of the lunar surface with highly oblique illumination conditions near the terminator. A series of pre-flight tests of LIC was performed. In those tests, the hardware performance and the functions of LIC were verified and the data for radiometric and geometric corrections were obtained. This paper outlines the scientific objective, characteristics of LIC, the procedure and the results of the pre-flight tests and the operation plan of LIC.

a) Kobe University, b) Institute of Space and Astronautical Science, c) Kochi University, d) Planetary Geological Society of Japan, e) Miyagi University of Education, f) Kyoto University, g) National Astronomical Observatory of Japan, h) National Institute for Environmental Studies, i) University of Aizu, j) University of Tokyo, k) National Institute of Advanced Industrial Science and Technology, l) University of Paris-Sud, m) Observatoire Mide-Pyrenees, n) NEC Toshiba Space Systems.Ltd, *) Emeritus

This document is provided by JAXA.

1. INTRODUCTION

The Japanese space mission, LUNAR-A, is designed to study the internal structures and evolution of the Moon by means of the "penetrators", which observe moonquakes and heat flux at the lunar surface, and by Lunar Imaging Camera (LIC) onboard the orbiter. The LUNAR-A spacecraft is spin-stabilized and orbits the Moon at altitudes of 200-300 km to relay data from the penetrators after they are separated from the spacecraft and deployed beneath the lunar surface for about a year. From this Data-relay orbit, LIC takes images of selected areas in the low- to mid-latitude regions of the Moon.

LIC is a monochromatic visible camera. The spacecraft spins about the axis pointing approximately toward the Sun. The camera has a linear CCD placed parallel to the axis, and obtains an image using the spin motion. Therefore, the camera takes images in the orientations nearly perpendicular from the Sun. This geometrical constraint allows us to recognize subtle selenomorphological undulations in the images with oblique solar illumination near the terminator. When the spacecraft altitude is 250 km, the spatial resolution of an LIC image is about 25 m/pixel at the surface of the Moon.

The LIC images are comparable with or better than the images in resolution obtained by the Lunar Orbiter, Apollo and Clementine missions. The cameras onboard the Clementine spacecraft globally mapped the Moon in 11 colors at an average surface resolution of about 200 m/pixel (Nozette et al. 1994). Photographs with much better resolutions were taken by the onboard cameras of the Apollo series. However, the photographed areas were limited by the short mission time. The highest resolved images for the remaining regions were taken by the Lunar Orbiter missions (Trask and Rowan 1967). The spatial resolution was from 60 to 100 m for most of the nearside of the Moon and from 150 to 300 m for most of the farside.

LIC is not aimed at global mapping, but is designed to obtain thousands of high resolution images of specific areas in low- to mid-latitude regions, where the spatial resolution of the previous images were not sufficient to investigate the topography and optical properties of the lunar surface. This article outlines the scientific objectives in section 2 and specification of LIC in section 3. The results of the pre-fright tests are reported in section 4 and an operation plan of LIC is presented in section 5.

2. SCIENTIFIC OBJECTIVES

The scientific objectives of the LIC observation cover impact craters, tectonic features, volcanic features, and photometric properties of the surface material and texture. In this chapter we give a brief outline and focus on some of topics for each of the above targets.

2. 1. IMPACT CRATERS

High-resolution images of LIC enable us to study the statistics and morphology of small craters. Detailed geologic and geomorphologic studies of large basins and complex craters by LIC will provide constraints on the cratering mechanisms, ejecta material distribution, pre-impact target structure, and post impact evolutional processes.

(1) Regional crater chronology by small impact craters

Age of the lunar surface is mostly estimated from a population density of craters on the area. Using low-resolution images, on relatively younger surface, lack of large craters makes it difficult to determine precise age. Moreover, a crater counting on images taken at high sun lighting conditions (e.g. Clementine UV-VIS) has difficulty in recognizing small craters. With oblique illumination, small bowl-shaped craters can be recognized by 3-4 pixels on surface images.

This document is provided by JAXA.

Therefore, near terminator observation by LIC may detect more numbers of 100 m (or less than 100 m) sized impact craters. These small craters are also of interest in study of the secondary crater population around primary craters (Vickery 1986; 1987). It is also preferable to examine the albedo of the ejecta for each crater. Since the space weathering timescale on lunar surface is 10^9 yrs, younger craters with high albedo should be picked up by LIC, which would give more constraint on the age determination.

(2) Regolith thickness determination from morphology and population of small impact craters

Lunar surface is covered with soil layers called regolith of a few m to a few 10 m in thickness. Regolith is composed of fine ejecta from impacts. Previous studies of regolith thickness are the estimations by Apollo seismometer, electromagnetic measurements by Apollo's lunar rover, and radar sounding from Apollo orbiter. However, measured area was very limited and there were no data on the farside of the moon, although there would be a large variation of regolith thickness on the surface.

It was proposed that size distribution of small craters should be largely affected by regolith thickness (Schultz et al. 1977). Whereas small-scale impact craterings on thick regolith are not affected by substrata, impacts on thin regolith are affected by the mechanically stable ones. For this project, high-resolution images should be taken at low spacecraft altitude (in the Penetrator separation orbit; see section 5) as many as possible.

(3) Structure of Orientale basin

Orientale basin is a huge young impact basin with a diameter of 930 km centered at 20° S and 265°. It has a well-preserved multi-ring structure. The central part with 320 km radius is covered by lava and called Mare Orientale.

Using LIC images taken at moderate solar illumination angle, multi-ring structure of Orientale will be investigated. In this ring system, prominent circular inward-facing scarps surround the central mare. The ring scarps become disorganized outside. High resolution imaging by LIC may constrain mechanism of ring structure formation. Crater age estimate is applied to lava between ridges consisting of ring structure. LIC can also investigate the topography of the central mare and clarify the volcanic activity that filled Orientale basin. Using images at low solar altitude, LIC may investigate the volcanic structure such as lava flows, domes, channels and pits. LIC may reveal tectonic features on the surface of the lava mare. Discussions on the tectonic features will be presented below.

2. 2. TECTONIC FEATURES

Ancient tectonic activities left their surface manifestations on the Moon, e.g., mare ridges (Howard and Muehlberger 1973, Lucchitta 1976, Sharpton and Head 1988, Horz et al. 1991) and arcuate rilles (McGill 1971, Head 1974, Golombek 1979). Many of those structures lie in low- and mid-latitude regions (Maxwell et al. 1976, Wilhelms 1987), where LIC takes high-resolution topographic images.

The tectonic features are clues to global thermal history (Solomon et al. 1976; Solomon 1977, Schubert et al. 1986, Kirk and Stevenson 1989) and further to the origin of the Earth-Moon system (Solomon 1986). Based on photogeologic investigations, Lucchitta and Watkins revealed that extensional tectonics ended on the Moon 3.6 ± 0.2 billion years ago, and horizontally compressional tectonics has prevailed thereafter (Lucchitta and Watkins 1974). High-resolution images that LIC acquires can be used to test this timing.

Mascon basins have mare ridges, and are encompassed by arcuate rilles. Those concentric structures suggest that the basins have intrinsic tectonism (Baldwin 1963, Maxwell et al. 1976). The formation of the structures is attributed to lithospheric flexure by the loading of mare deposits, and is used to estimate the ancient strength of the lithosphere, probably increased by global cooling (Solomon and Head 1979; 1980, Freed et al. 2001). High resolution LIC images are used to investigate the existence of strike-slip faults, possibly activated by the loading (Melosh 1978, Freed et al. 2001).

This document is provided by JAXA.

Tectonic features are also clues to the orbital evolution of the Moon, as lowering tidal bulges, due to the Moon's recession from the Earth, can produce so large horizontal strain that is visualized by the features (Melosh 1980). Lineament patterns do not support this hypothesis (Chabot et al. 2000). However, the detailed investigations of mare ridges and grabens are needed for understanding the strain field, as lineaments not always designate strain. LIC images are useful for this purpose.

2. 3. VOLCANIC FEATURES

Volcanic features include lava flows, domes, cones and sinuous rilles. Some of them are already introduced in the above. Dome-like features are ubiquitous in the maria of the lunar equatorial region. Over 200 dome-like features have been known. They are flat, generally circular in structure with convex shape, having slopes less than about 5° and displaying summit craters. The high-resolution images of LIC taken with oblique illumination will reveal detailed structure of domes (flow fronts, levees, vents), which can give new constraints on the process of dome formation.

2. 4. PHOTOMETRIC PROPERTIES

Brightness of lunar surface depends on both properties of surface material and the viewing and illumination geometry (Hapke 1981, McEwen 1991, Kreslavsky et al. 2000). The observational geometry is generally defined by three parameters: incidence angle i, emission angle e, and phase angle α (Figure 2-1). Based on Kreslavsky et al. (2000), semi-empirical photometric model for lunar surface is rewritten as

$$F(i, e, \alpha) = A \cdot D(i, e, \alpha) \cdot f(\alpha), \qquad \text{(Eq.2-1)}$$

where F is the observed intensity, A is the term dependent on albedo (A also corresponds to $F(30°, 0°, 30°)$), D is the term dependent on the viewing parameters, and f is the term dependent on α which is traditionally called as "phase function".

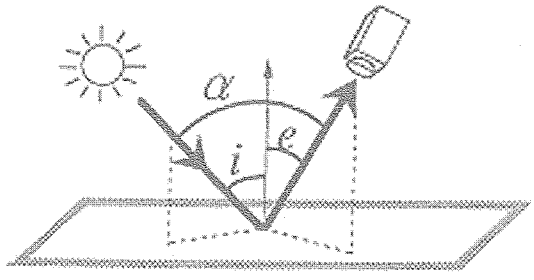

Figure 2-1 Basic geometry angles.

The observed $F(i, e, \alpha)$ should be corrected to A to discuss mineralogy of the lunar surface. However, both D and F are not yet fully understood due to the limited range of parameters of observational geometry achieved in each spacecraft mission (e.g., Clementine's nominal observation was conducted only in the parameter range of $0° < \alpha < 90°$, $0° < i < 90°$, $0° < e < 0.5°$). In addition, comparison of this equation with theoretical model (Hapke 1981, Hapke 1984) indicates that they reflect various factors such as scattering, absorption and macroscopic roughness of the surface. Thus studies on these characteristics will also contribute to the understanding of grain size and packing status of the lunar regolith.

LIC observes lunar terminator area under the various viewing geometry by using its spin motion. Table 2-1 summarizes the range of i, e, and α for LIC (see Appendix A-1 and A-2 for more detailed description). The characteristic of LIC's observational geometry is a wide range of e, which enables a detailed study of lunar optical properties. Furthermore, integration of LIC's observation with those of the other missions such as Clementine UVVIS

This document is provided by JAXA.

camera and SMART-1 camera (Asteroid-Moon micro-Image Experiment: AMIE, Pinet et. al., 2005) will contribute to the better understanding of lunar optical properties.

Table 2-1 The range of parameters of viewing and illumination geometry for LIC.

Parameter	Range
incidence angle i	0° - 90°
emission angle e	0° - 90°
Phase angle α	52.7° - 127.3°

(#) As shown in Figure 2-1, the values of i, e and α are interdependent through the relationship that α equals the complement of the angle between incident vector and emission vector ($i+e \geq \alpha$).

As for more detailed scientific objectives, four photometric studies are proposed: (a) study of directional scattering property of the regolith, (b) measurement of roughness of lunar surface, (c) application of photoclinometry for topographic study, and (d) compositional distribution. The details of each study are described in the following.

A. Directional scattering property of the regolith:
Directional scattering property of the regolith relates to phase function (Hapke and Wells 1981) and thus $f(\alpha)$ in equation 2.1. Studies on this property require observation of lunar surface in a wide range of phase angle α. Integration of LIC data and other missions' data will improve our knowledge of lunar phase function.

B. Roughness of lunar surface:
When the incidence angle or the emission angle becomes very large (~90°), surface roughness of the regolith layer affects the photometric behavior (Hapke 1984). Images around the lunar terminator taken by LIC will contribute to study this effect.

C. Application of photoclinometry to topographic study:
Images taken at moderately large incidence angles make recognition of topographic feature easier than those at small incidence angle. Using semi-empirical photometric models (McEwen 1991, Kreslavsky et al. 2000), spatial difference of the light intensity in the image can be interpreted to as the deviation of the incidence and emission angles due to surface irregularities. Thus undulation of the surface can be derived quantitatively from this deviation. Such method is called as photoclinometry, and useful for topographic study. To improve the accuracy of the photoclinometory, an empirical function must be established for typical lunar surface. LIC images of areas where Apollo mission already derived elevation maps are appropriate for such examination and thus useful for improvement of photoclinometric studies.

D. Compositional distribution:
In mature regolith, the composition strongly affects the albedo (Wilhelms 1987). Contrast between different materials shows up best at the incidence angle smaller than 45°. LIC images taken under small incidence angle can be used to study compositional distribution. However, such observation will be very restricted for LIC because of its monochromatic band and the increase of the slant distance between the target area and the camera at smaller incidence angle, thus this should be complemented by observation by other mission, such as UVVIS of Clementine and AMIE of SMART-1.

Figure 2-2 summarizes above targets of photometric studies by LIC and shows the relationship among them as a flow diagram.

This document is provided by JAXA.

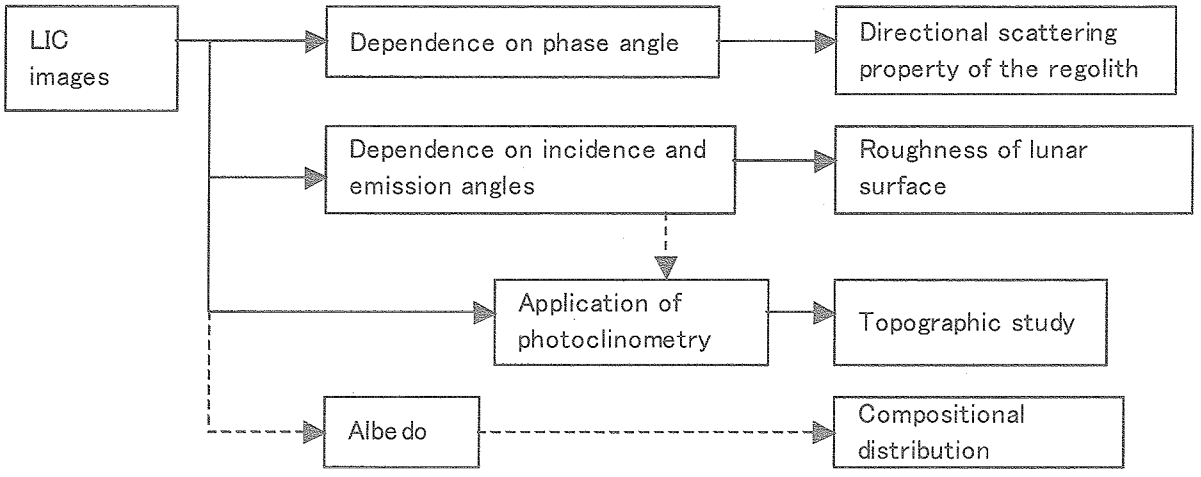

Figure 2-2 Outline of optical characteristics study.

3. INSTRUMENT OVERVIEW

LIC has been designed and developed in parallel with Mars Imaging Camera (MIC) (Ninomiya et al. 1999) that is onboard the Japanese Mars mission, NOZOMI, launched in July 1998. Both cameras are small, compact, lightweight, have linear sensors placed parallel with the spin axis of the spacecraft, and take two-dimensional images using the spin motion of the spacecraft. LIC is a monochromatic camera, whereas MIC can take images in three colors. Originally, both cameras were designed to function in an "autonomous tracking mode" and an "auto-imaging mode" in preparation for encounters with small bodies, such as the Martian satellites, Phobos and Deimos. In autonomous tracking mode, the camera will track an object moving relative to the spacecraft by analyzing its motion. In auto-imaging mode, the camera detects a bright object defined by a threshold brightness level. Since these functions were tested and evaluated on MIC in the Earth-Moon orbiting phase of the NOZOMI spacecraft, these modes were removed from the functions of LIC. Other major differences from MIC are the use of a data recorder on the spacecraft (lunar data processor, LDP), while MIC stored images in its own image memory, and all the power is supplied from a common source (power controller and distributor, PCD) on the spacecraft, while MIC was equipped with a secondary power source.

3. 1. COMPONENTS

LIC, shown in Figure 3-1, consists of an optical system (CCD-ASSY) and an electronic box. The electronic box consists of five printed wiring boards (PWBs), an ASP1 (analog signal processor)-PWB, an ASP2-PWB, a DSP (digital signal processor)-PWB, a JPEG-PWB, and an SIP (SI-CPU processor)-PWB. Elastomeric connectors inlaid in the frames are used to connect circuits between the PWBs. Chip packages are used for most of the electronic parts and the frames are constructed from a magnesium alloy to reduce the weight of the electronic box. Figure 3-2 shows the configuration of LIC. The specification and characteristics of the instrument are summarized in Table 3-1, and each of the components will be described in the following sections.

This document is provided by JAXA.

Figure 3-1 The lunar imaging camera

Table 3-1 Specification and characteristics of LIC

Optics	Refractive system Focal length: 70mm±2%, Aperture: 50±0.2mm, F number: 1.4 Wavelength range: 420 - 680 nm (FWHM) Total MTF*1): > 0.1 (at Nyquist frequency) Distortion: <2% Vignetting: better than 30% of the center Transmissivity: more than 60% on average for 480-700nm
Total FOV	360 (azimuth: around the spin axis)×14.6° (elevation: along the line of the CCD)
CCD	NEC μPD35H71 2560 pixels are used out of a total of 5000 pixels Pixel size: 7 (azimuth)×7 μm (elevation)
Integration time	0.3072 ms
Angular resolution	19.9-39.8/pixel (azimuth, at 3-6 rpm)×20.6"/pixel (elevation, at the center of the FOV)
Gain	Factor (Mode): 2.36 (Gain0), 6.3 (Gain1), 12.6 (Gain2), 15.75 (Gain3) Linearity: deviance is less than ±5%
A/D Conversion	Dynamic range: 8 bits, Rate: 10 MHz
S/N	More than 64 (6bits) for the Gain3 full scale (8bits) *2)
Image memory	1 Mbytes
Image size	Alternatives 1024×1024, 512×2048, 2048×512, 1024×512, 512×1024, and 512×512
Onboard image processing	Non-reversible compression (JPEG revision 5) and odd-even pixel separation
CPU	80C86 8 MHz
Temperature control	30±3°C for optics
Size	213.5×120×280 mm^3
Weight	2.5±0.1 kg
Power consumption	11.9 W (max)

*1) Including the alignment error of the CCD and the analogue signal processing
*2) The required noise level is less than 4 LSB.

This document is provided by JAXA.

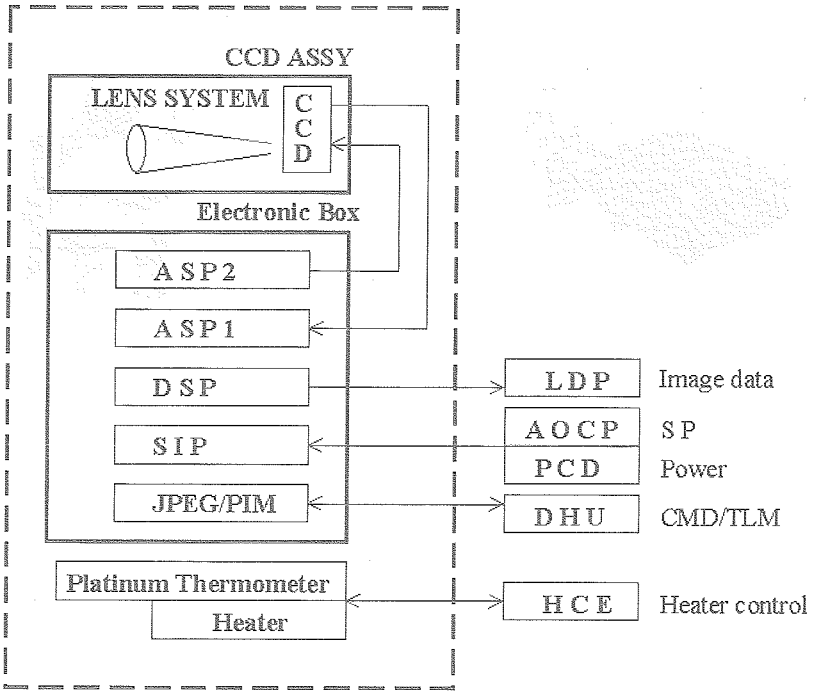

Figure 3-2 Configuration of LIC. The dashed line encloses the components of LIC.

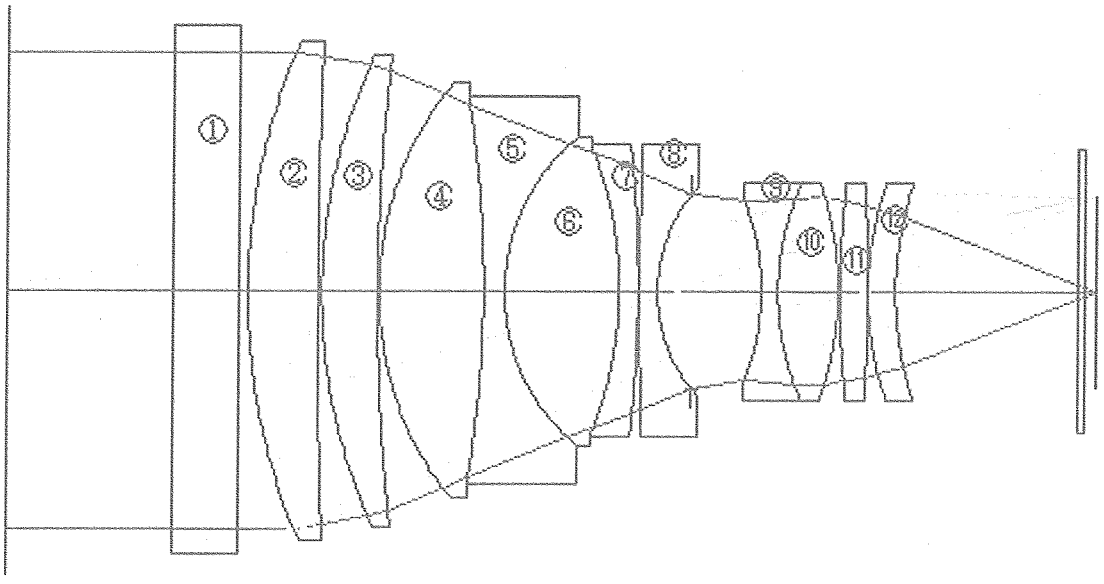

Figure 3-3 Layout of LIC lens system (②-⑫) and a glass window (①). The bar in front of the CCD (right most) illustrates a slit on the CCD-mask. The effective diameter of the first lens next to the optical parallel windows is 50 mm. A macro slit is placed parallel to the CCD and in between the slit and the rearmost lens (⑫) .

This document is provided by JAXA.

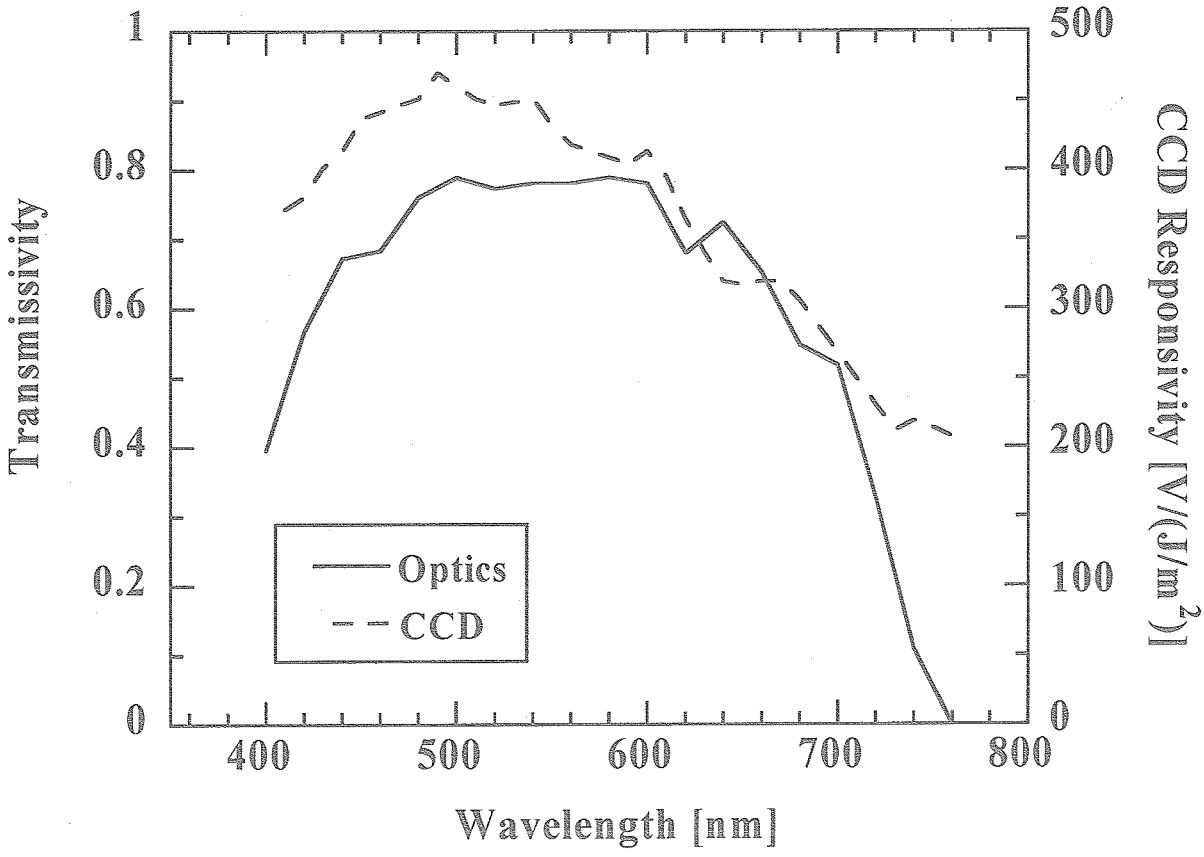

Figure 3-4 Spectral responsivity of the system.

The CCD-ASSY consists of a lens-system and a CCD-PWB. The CCD-PWB consists of a linear CCD image sensor and a pre-amplifier. The optics is an assembly of eleven lenses. The focal length, aperture, and F-number are 70 mm, 50 mm, and 1.4, respectively. The chromatic aberration is minimized by using two extraordinary dispersion (ED) lenses. The spot diameter on the optical axis is 6 μm. Figure 3-3 shows the layout of the lenses and Figure 3-4 shows the spectral responsivity of the system. Just in front of the first lens, a non-browning glass window is placed for radiation tolerance. The transmission efficiency of the optics is the measured values of the flight model and the CCD responsivity is the value measured for a similar product of the same type by the manufacturer. The temperature of the telescope is controlled by a heater at 30±3℃ in order to keep the change of the focal length within 10 μm.

The image sensor is an NEC μPD35H71. The sensor consists of 5,000 active pixels. Approximately half (2,560) of the pixels are used for imaging and the rest are masked. A plate with a macro slit is placed between the optics and the CCD-PWB to reduce the stray light reflected by the electronic parts on the CCD-PWD. The CCD array is placed parallel to the spin axis of the spacecraft. The center of the field of view (FOV) points in a direction orthogonal to the spin axis. The imaging coordinates are such that the azimuth and elevation are the directions around the spin axis that correspond to a phase angle of the spacecraft's spin and the direction along the CCD line, respectively. Figure 3-5 shows the coordinate system of the imaging. The height and pitch of the pixels are both 7 μm. The integration time is fixed at 0.3072 ms, which yields an angular resolution (azimuth) of 20 arcsec at the nominal spin rate, 3 rpm, although the resolution of the azimuth direction depends on the spacecraft spin rate. The total FOV is 360 ×14.6° (azimuth×elevation). The very short integration time guarantees a negligible level of fluctuation of the dark current

This document is provided by JAXA.

on the CCD. The CCD is not cooled and is thermally combined with the telescope so that it will operate at almost the same temperature as the telescope. LIC has no hood, but the solar paddle of the spacecraft prevents direct irradiation of the optics by the sun.

The ASPs are analog circuits, fine-tuning the driving signal of the CCD, processing the analog signals from the pre-amplifier in the CCD-PWB, and performing the analogue-digital (A/D) conversion. The signal is amplified by gain-amplifiers to one of four levels and an offset voltage is added before A/D conversion. The signal digitization is 8 bits.

The DSP-PWB consists of a hardwired command (CMD) decoder, an output circuit for the telemetry (TLM), a circuit for the driving signal of the CCD, 1 Mbytes image memory, a multiplexer for the analogue housekeeping (HK) data, an interface circuit for the LDP, and a dynamic random access memory (DRAM) controller for transferring the image data. The digitized image data are stored in the 1 Mbytes memory on the DSP-PWB.

The SIP-PWB is a CPU-board developed for scientific instruments on the NOZOMI mission. It consists of a CPU (80C86 8 MHz), a timer, an interrupt controller, a clock generator, a command decoder for the CPU, an A/D converter for the analogue HK, a latching circuit for the A/D converted data, a telemetry output circuit, and a 512-KB static random access memory (SRAM) for storing the program and the working area. The software on the SIP handles commands from the main CPU of the spacecraft (data handling unit, DHU) and telemetry, controls the camera, and manages the image memory. The information related to the imaging conditions is stored in the working area of the software and will be added to the image as "picture headers" when the data are transferred to LDP.

JPEG-PWB consists of circuits for an image compression module (ICM) and a peripheral interface module (PIM). The HK telemetry data is provided to DHU through the PIM. The ICM was supplied by the Centre National d'Etudes Spatiales (CNES) of France and uses a JPEG rev.5 image compression that is a standard non-reversible compression algorithm. The module formats the rasterized data into an 8×8 pixels block, performs the discrete cosine transform, quantization, Huffman encoding, and formatting. The quantization matrix and scale factor controlling image quality are selectable as image compression parameters.

LIC measures $213.5 \times 120 \times 280$ mm^3 and weighs 2.5 kg. The analog circuits are usually off to save power and to suppress a rise in the temperature of the instrument. The analog circuits are turned on only when taking images. Therefore, the power consumption of LIC is usually 8.5 W and during imaging, it is 11.9 W, maximally. The power consumption of the heater for the telescope temperature control by heater control electronics (HCE) is not included here. The CCD can be driven for only 20 minutes running to prevent an increase in the temperature of the CCD and the lens-system, according to a thermal analysis.

This document is provided by JAXA.

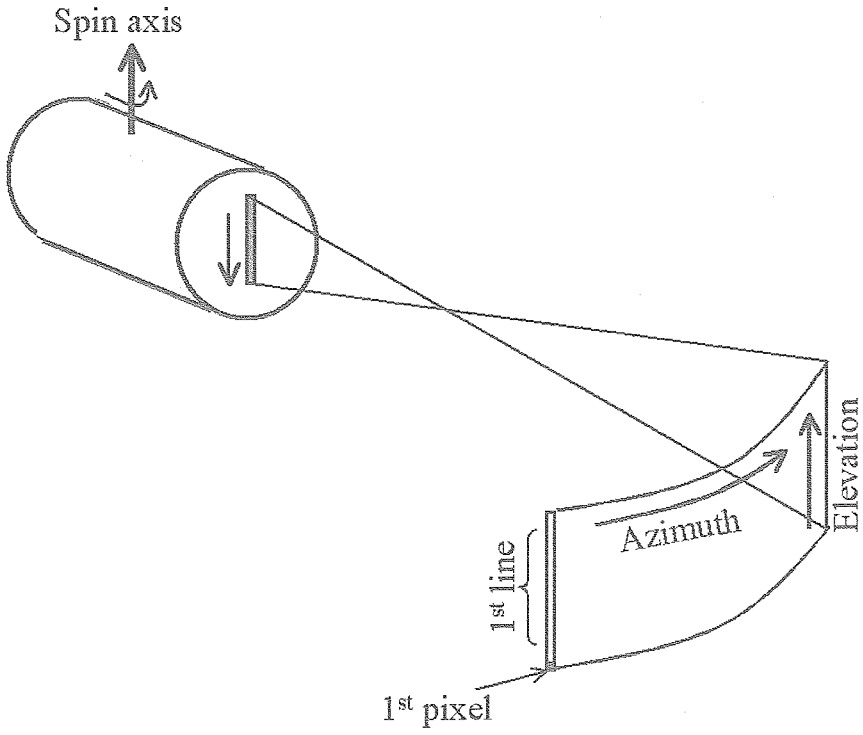

Figure 3-5 Coordinate system of LIC imaging. The spin axis points approximately toward the Sun. See also Appendix.

3. 2. FUNCTIONS

LIC takes an image of a designated area in the total FOV. The start angle is set at 512 lines per interval. The elevation angle is defined by the start pixel and is designated at 128 pixels per interval. The image size can be chosen from 512 ×512, 512 ×1024, 1024×1024, 512 ×2048, 1024×512, or 2048×512. The gain modes are Gain0 (lowest), Gain1, Gain2, or Gain3 (highest). The alternative gain factors are designated 2.36, 6.3, 12.6, and 15.75, respectively.

There are three alternatives in the image compression mode: raw original image only, raw image with compressed image, or compressed image only. The quantization matrix is selected from the two available alternates. The scale factor can be specified from sixteen (16) grades. Image compression is performed for either the original image or the rearranged image, in which the signals from the odd and even pixels are separated. This mode will be useful when the difference in the offset levels of the odd and even pixels, hereafter referred to as the "odd-even difference", becomes large in flight.

These imaging parameters are designated by the MODE_SET command. The MODE_SET commands are transmitted to the command buffer of LIC before the imaging operation initiated by a TAKE command. The maximum number of MODE_SET commands storable in the buffer is sixty-four (64), corresponding to the maximum number of images (64) designated by one TAKE command.

3. 3. IMAGING OPERATION

The signals from the CCD are processed as follows: signals from the odd and even pixels of the CCD are pre-amplified separately and clamped, and then merged through a multiplexer. The designated part of the analogue signals are converted to 8 bit digital signals and then stored in the 1 Mbytes image memory. When image

This document is provided by JAXA.

compression is indicated by a command, the data in the memory are transferred to the ICM by the direct memory access (DMA) controller, compressed by the ICM and then transferred back again to the image memory by the DMA controller. When the LDP_OUT_ENABLE command is issued, the data are transferred to the LDP interface, and eventually sent to the LDP as serial data with a picture header.

When the SI-CPU receives a TAKE command from the DHU, it then reads a MODE_SET command from the command buffer and applies the imaging parameters indicated in the arguments of the MODE_SET command to the camera and then sends the TAKE command to the DSP. The camera is triggered by the first Sun Pulse (SP) issued by attitude and orbit control processor (AOCP) and performs the imaging and image compression. LIC reads the MODE_SET commands from the buffer sequentially and continues imaging at every succeeding spin until the total number of images reaches to the value given by the argument of the TAKE command. In the sequential imaging process, the second and all subsequent images are taken without waiting for a new SP to be issued, but at the spin phase designated by the MODE_SET command.

The maximum amount of data that the LDP can receive per spin, or more accurately per fifteen seconds, is 256 Kbytes. Therefore, when an image with the picture header exceeds this limit, the data transfer is not finished within a spin. The image transfer to the LDP is one by one, even if the image is very small, i.e., only one image can be transferred within a spin. The raw image is treated separately from the compressed image, when both the raw and compressed images are to be transferred; the raw image is transferred first and then the compressed image is transferred by the next spin. Due to these constraints, the nominal operation of LIC is sequential imaging with moderate image compression without the storage of the raw image. The compressed image with the picture header should be less than 256 Kbytes.

4. PRE-FLIGHT TESTS

The pre-flight tests consisted of electrical and optical performance tests of the camera and environmental tests of the subsystem and integrated spacecraft. All the sensor-level tests were completed by the end of spring, 2004. Table 4-1 lists the test items.

Electrical performance tests examined the dark-offset-level (hereafter, the dark level), the odd-even difference, and the signal-to-noise (S/N) ratio. Imaging of any object is simulated by taking an image of fluorescent light. Proof that the camera operated according to the commands was thoroughly verified using HK telemetry data and image data. As some of the camera functions could be tested only with other instruments on the spacecraft, electronic interface tests were conducted with other instruments.

Optical performance tests were used to characterize the performance and to provide the calibration factors for converting the data into physical units. Alignment, modulation transfer function (MTF), and distortion were measured using a collimator. Vignetting, the relative sensitivity of the pixels, linearity, amp-gain factors, and the absolute sensitivity of the system were determined using an integration sphere. Both of the measurement systems were prepared in clean rooms at NEC Toshiba Space Systems (NTS). The flatfield of the camera will be confirmed and revised using a new flatfield image synthesized from numerous lunar images. Conversely, in-flight absolute calibration using stars is not expected owing to the low sensitivity of LIC, which is tuned to the brightness of the lunar surface.

Mechanical environmental tests included random vibration, point shock, and drop shock tests. The camera operation and performance were tested before and after each test. In the qualification tests (QT) for LIC, random vibration and point/drop shock tests were performed at the 1.5 times longer time and higher levels than those

This document is provided by JAXA.

predicted during the real-flight operation, whereas the duration and stresses are equal to the predicted orbit environment in the acceptance testing levels (AT).

The temperature dependence of the performance was tested in two ways. Before subsystem integration, the dark level, flatfield, and odd-even difference were studied by operating LIC in a temperature-controlled chamber. Then, in a series of subsystem environmental tests, LIC was operated in a thermal vacuum (TV) chamber, where its thermal mathematical model and the performance were checked.

This document is provided by JAXA.

Table 4-1 LIC test items

Items	Sub-system test			Integration test	
	Electrical performance test	Optical performance test	Environmental test	Electrical performance and spacecraft spin test	Environmental test
Electrical performance					
Dark level	○		○	○	○
Odd-even difference	○		○	○	○
Signal-to-noise ratio	○		○	○	○
Current consumption	○		○	○	○
Temperature dependence			○		○
Voltage dependence		○			
Imaging function					
Gain selection	○			○	
Image size setting	○			○	
Start line and pixel setting	○			○	
Dark imaging	○		○	○	
Object imaging	○		○	○	
Continuous imaging	○			○	
Imaging with spin motion				○	
Data processing					
CMD acceptance	○			○	
Telemetry transmittance				○	
Change of transfer rate to LDP	○			○	
Odd-even separation	○			○	
Compression	○			○	
Interface (I/F) functions					
LDP I/F				○	
PCD I/F				○	
HCE I/F					○
AOCE I/F				○	
DHU I/F				○	
Optical performance					
MTF		○	○		
Distortion		○			
Alignment		○	○		
2-dimensional chart		○			
Linearity		○	○		
Flatfield		○			
Absolute sensitivity		○			
Heater control of the optics		○	○		
Mechanical and thermal performance					
Random vibration tolerance			○		○
Point shock durability			○		○
Drop shock durability			○		○
Thermal vacuum tolerance			○		○
Dimension			○		
Weight and center of gravity			○		

Items with shading have not yet been evaluated.

This document is provided by JAXA.

4. 1. ELECTRICAL PERFORMANCE TESTS

LIC can take an image and transfer it to LDP each spin only when the image size including the picture header is less than 256 Kbytes. The nominal size of the image is planned to be 1024 pixels×1024 lines; therefore, the compressed image data should be less than 25% of the original image. The uncertainty of the data in LIC arises not only from the usual sources, such as Poisson noise from the light from the object, electronic noise, and quantization noise associated with A/D conversion, but also from the irreversibility of the data due to lossy compression, especially when enhanced by the odd-even difference. The difference in data number (DN) between the original and decompressed images is hereafter called the compression error.

Figures 4-1 and 4-2 show the typical dark level at each pixel averaged over lines, gain mode, and the standard deviation, respectively. The dark level was flat along elevation within 1 least significant bit (LSB), although there was a tendency to increase or decrease with elevation near the start pixel. The odd-even difference increased with the gain factors. The standard deviation was also within 1 LSB and met the S/N requirement. There was no distinct periodic noise in the image, except for a little noise in the contrast-enhanced images taken at Gain2 and Gain3. The timing of this noise was related to the operation of the PIM; therefore, we call it "PIM noise". Figure 4-3 shows an example of PIM noise. The peak-to-peak amplitude of the PIM noise was reduced to 2 (2), 5 (4), 10 (8), and 12 (10) LSB at Gain0, 1, 2, and 3, respectively, by adjusting the electrical circuits, where the numbers in parentheses are the mode values. Figure 4-4 shows the variation in the dark level with the temperature and ground conditions. We tuned the electrical circuits to minimize the odd-even difference at the temperature range expected in flight and validated the adjustments in the thermal vacuum test described in section 4-4.

Functions and data processing of LIC such as continuous imaging, image compression, odd-even separation, and so on were tested with dark and object images. Usually images of fluorescent light were taken instead of two-dimensional object images. Because the brightness of fluorescent light periodically varies with the alternating electrical power supplied to the light tubes, the LIC images of fluorescent light become the ones with bright and dark fringes. Figure 4-5 shows a typical image of fluorescent light.

This document is provided by JAXA.

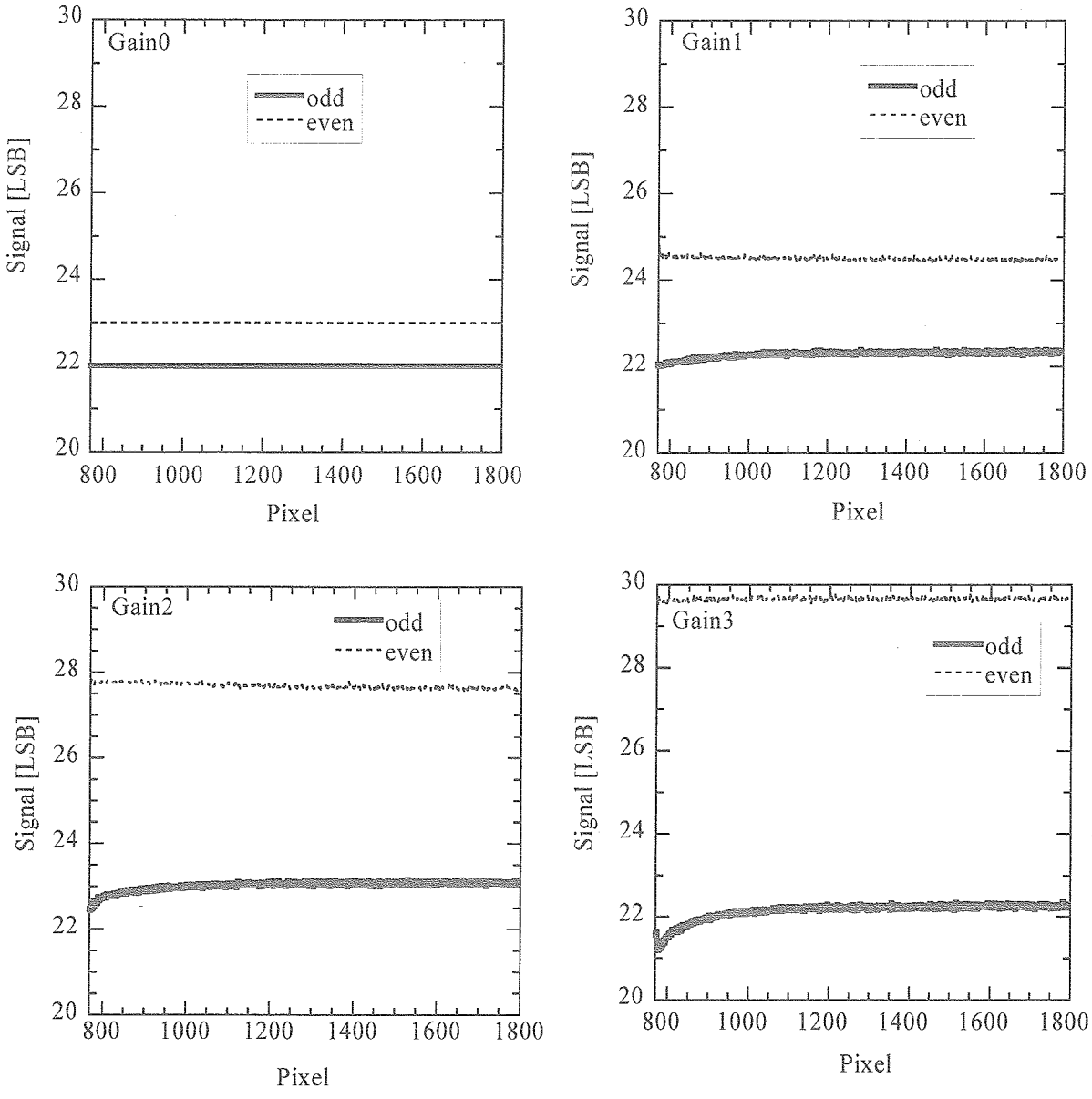

Figure 4-1 Dark level at each gain. The data were collected at room temperature. The start pixel was the 769th pixel.

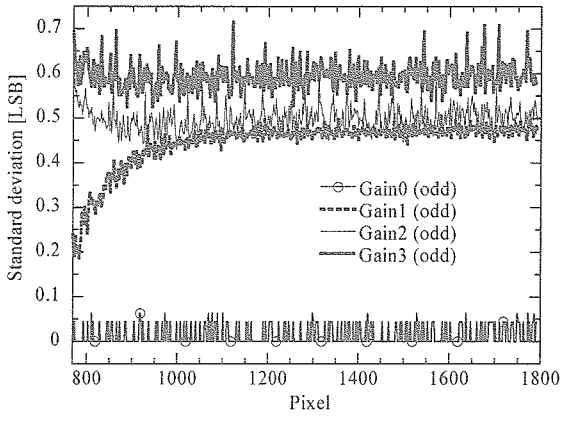

Figure 4-2 Standard deviation of the dark level at each gain.

This document is provided by JAXA.

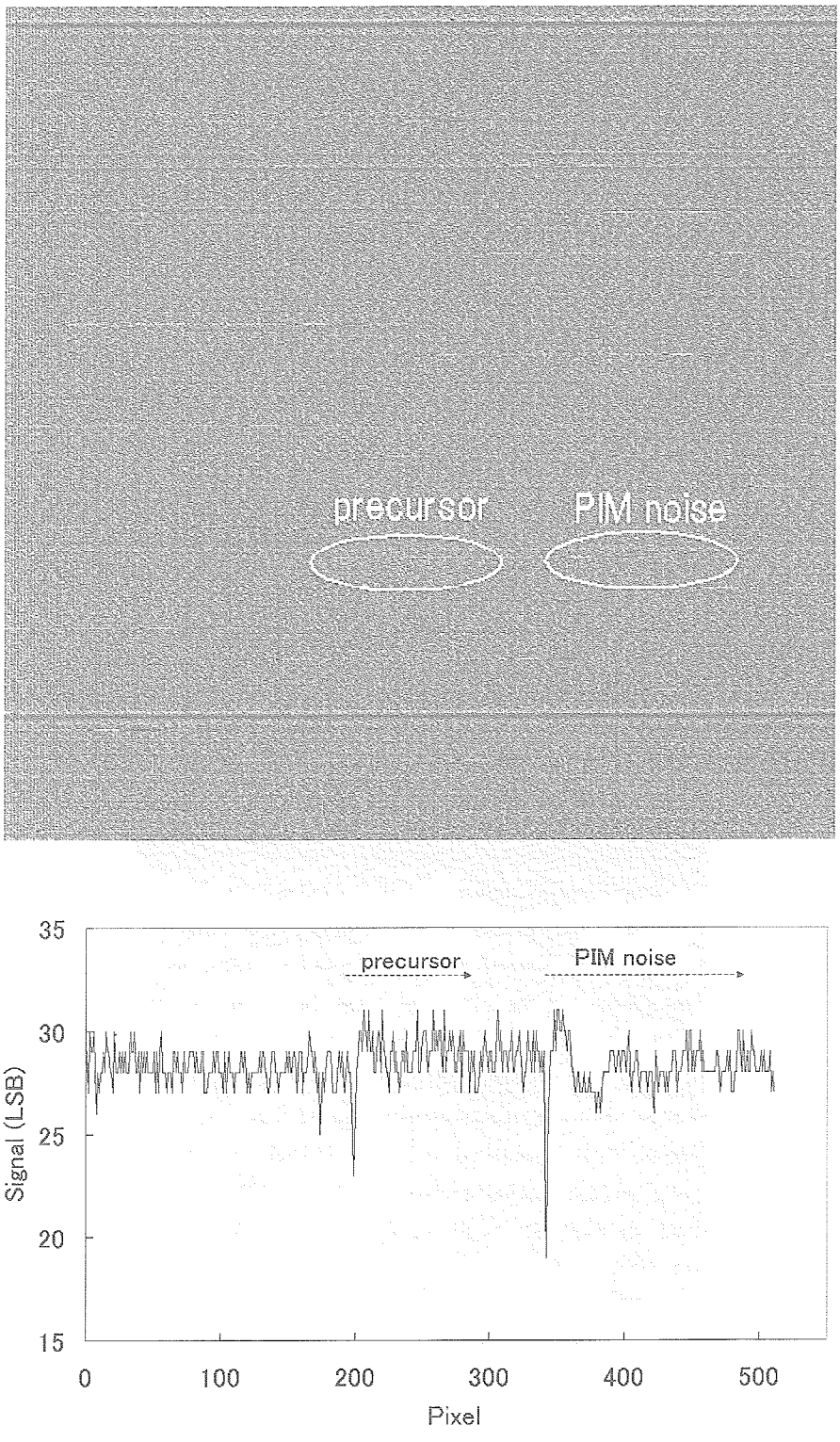

Figure 4-3 The upper is a typical dark image with PIM noises taken during the electrical performance test on May 26, 2004 (Gain3, image size 512 pixels×512 pixels, and the odd-even level difference and the contrast were adjusted). The lower shows the profile at 338-th line of the above image. PIM noise and its precursor are indicated in both. The sampling time for 100 pixels corresponds to 10 μ sec.

This document is provided by JAXA.

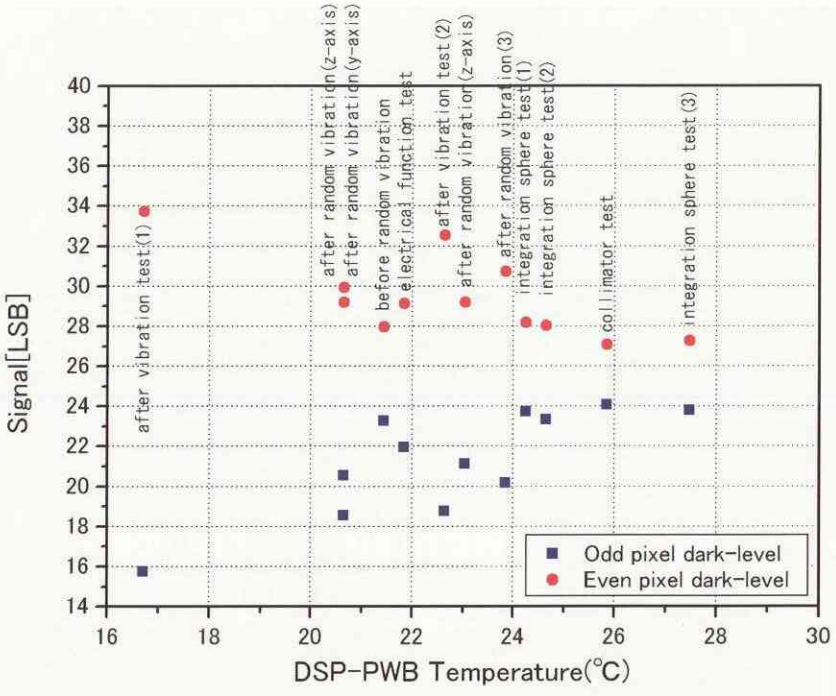

Figure 4-4 Variation in the dark level with temperature and the ground conditions. The temperature for each data point in the figure is a preliminary value.

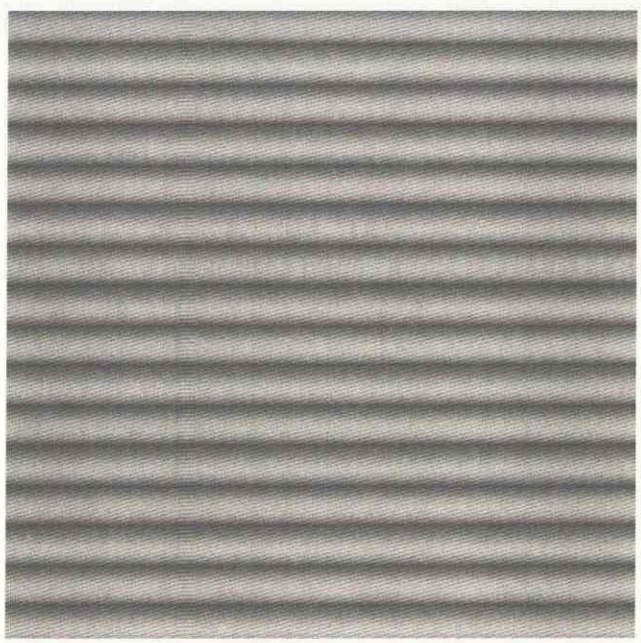

Figure 4-5 An example of fluorescent light image. Gain3, image size 512 × 512.

This document is provided by JAXA.

In the following, we show (1) the results of simulations of the relationship between the odd-even difference and the degree of compression error and compression efficiency. Next, we discuss (2) a simulation of the effect of the PIM noise on the quality of the decompressed images. According to these simulations, we verified the pre-flight levels of the odd-even difference and PIM noise meet the data quality requirements.

(1) Odd-even difference

We simulated the effect of odd-even difference on the quality of the decompressed image. Model LIC images were synthesized by adding the odd-even difference to brightness-modified UV-VIS images of the Clementine mission from Clementine EDR Image Archive (http://starbase.jpl.nasa.gov/archive/ clem1-l_e_y-a_b_u_h_l_n-2-edr-v1.0/), using the difference between the sensitivity of LIC and that of the UV-VIS camera. The model images were compressed and decompressed, and then compared with the original images pixel by pixel. The degrees of compression error were examined. Figure 4-6 shows examples of the UV-VIS images used in the simulation and the results. The *SNR* in the vertical axis is defined as

$$SNR = 20\log(255/n),$$
$$n = \sqrt{\sum \{DN(original) - DN(decompressed)\}^2 / N}, \qquad \text{(Eq.4-1)}$$

where *DN (original)* and *DN (decompressed)* are the data number of the pixel in the original and decompressed images, respectively, and *N* is the number of pixels in the image. The results were dependent on the original image, i.e., the brightness (DN value) distribution of the image. However, the general tendency was for (1) the compression error to decrease more for usual compression than for odd-even separated compression, when the odd-even difference was smaller than 10 LSB, and (2) topographical features could still be identified after decompression when the odd-even difference was less than 7 LSB.

This document is provided by JAXA.

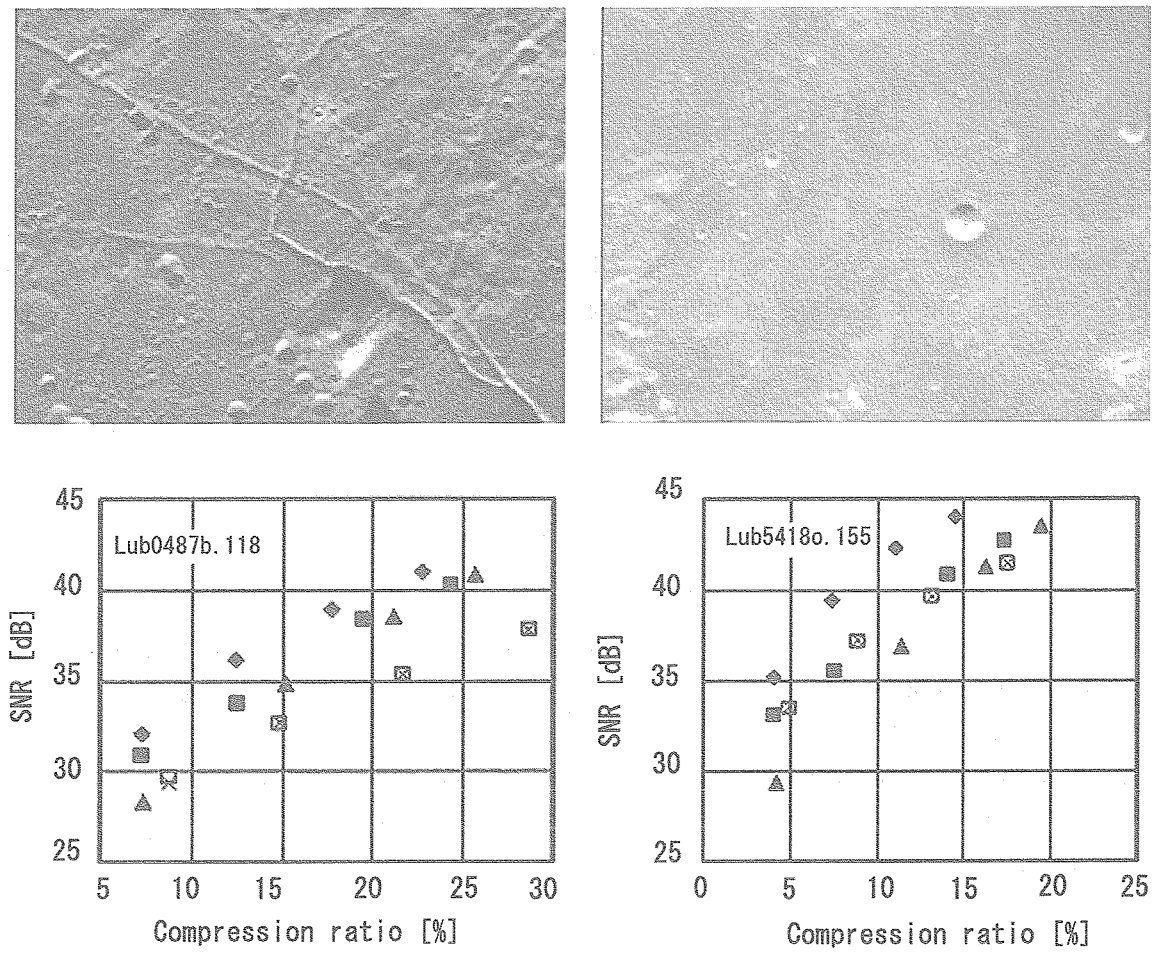

Figure 4-6 UV-VIS images used in the simulation and the results of the simulation. The upper images are Clementine UV-VIS images that were used in the simulation: Lub0487b.118 (left) and Lub5418o.155 (right). The solid diamonds, squares, and triangles are the cases in which the standard (odd-even non-separated) images were compressed, whereas the open squares and crosses show the cases where odd-even separated images were compressed. The odd-even differences of the solid diamonds, squares, and triangles were 0, 7, and 15 LSB, respectively. The odd-even differences of the open squares and crosses were 0 and 7 LSB, respectively, and the SNR for both cases was essentially in agreement.

We performed a detailed study of the relation between the compression ratio and the error by changing the odd-even difference. Figure 4-7 shows the results of the analyses. The LIC images will nominally be compressed to 15-20% of the original images, as noted in the previous section. With such a compression ratio, the degree of compression error differs between cases where the odd-even difference is less than 3 LSB or more than 5 LSB. When the odd-even difference is less than 5 LSB, the compression error is only 2-3 LSB and is not far from the levels of other errors.

This document is provided by JAXA.

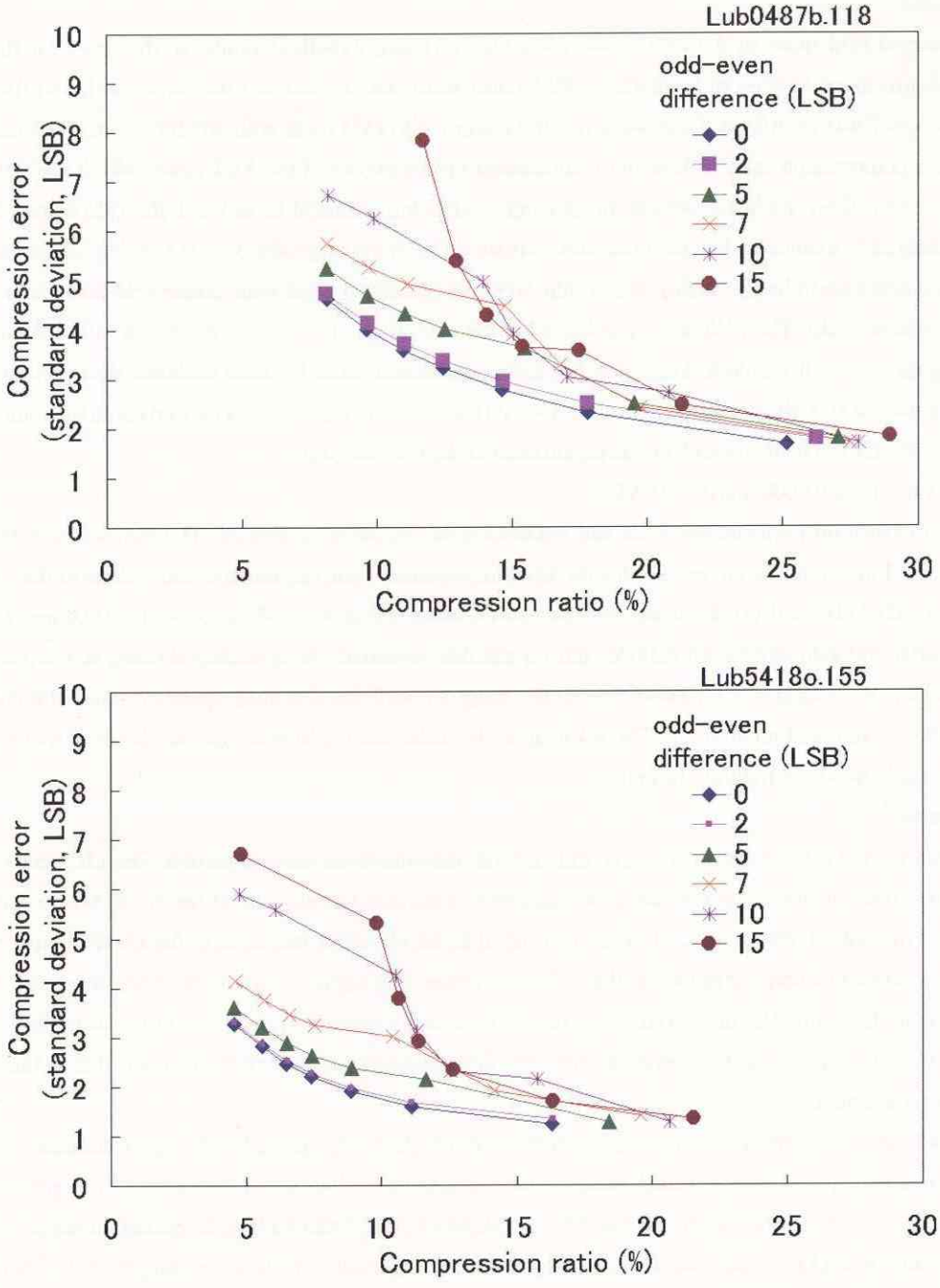

Figure 4-7 The relationship between the compression error and the compression ratio for various odd-even differences. The upper figure shows the results of the simulation with Lub0487b.118 and the lower figure shows the simulation for Lub5418o.155.

This document is provided by JAXA.

(2) PIM noise

The effect of PIM noise in the compression was studied using a method similar to that used for the odd-even difference. Synthesized images with simulated PIM noise were compressed and decompressed, and the degree of compression error was examined. First, we simulated images with PIM noise with amplitudes of 20-25 LSB (peak-to-peak). With a compression ratio of 10%, the compression errors exceeded the PIM noise, which was buried in the compression error. Conversely, for weaker image compression with ratios of 18 and 25%, the PIM noise was restored in the decompressed images with almost the same amplitude as in the originals, despite the degradation of shape. In these cases, a decrease in image quality was visible. Next, we simulated cases with fainter PIM noise with amplitudes of 10 LSB (peak-to-peak). The PIM noise was buried in the compression errors in the images with 18% compression, while remnants were still visible in images with a 25% compression ratio. Detailed analyses showed that PIM noise with an amplitude of 10 LSB was marginally buried within the $\pm 2\ \sigma$ compression error and could be neglected in 20% compression, which will be the default compression ratio of the LIC imaging.

4. 2. OPTICAL PERFORMANCE TESTS

A series of ground performance tests and calibration of LIC were conducted. The purpose was to verify the performance and to define the characteristics required for geometric and radiometric corrections of the images. The (1) alignment, (2) MTF, and (3) distortion were measured using primarily a collimator with a 3,000 mm focal length. The (4) linearity and gain factors, (5) flatfield, and (6) absolute sensitivity were measured using an integration sphere 2 m in diameter. We obtained a (7) two-dimensional image for verifying the image polarity, using the collimator by moving a chart of an aerial photograph. The (8) magnitude of the stray light from outside the FOV was estimated by attaching a simple hood around the LIC optics.

(1) Alignment

The alignment of LIC was verified before and after the environmental tests as follows. The LIC optics was placed on a rotation and inclination stage that faced the collimator beam using a cube mirror on its CCD-ASSY (see Fig. 3-1). The center of the optical axis of the CCD was determined in the elevation and azimuth directions by inserting charts with a narrow horizontal and vertical slit in the collimator beam. The axes $\pm 7^{\circ}$ from the center were also determined for the elevation direction. The measurement error was expected to be within $\pm 15\ \mu$m in the azimuth direction and $\pm 15\ \mu$m added on ± 1 pixel in the elevation direction. The dominant measurement error was due to the adjustment of LIC on the test bench.

Table 4-2 shows the results of the alignment measurements before and after the environmental tests. All the measurements were performed in Gain1 mode. There was a larger than expected change in alignment after the vibration and shock tests (QT, 3-axis, see section 4.3). However, there was no further change in alignment after the random vibration test (AT, 1-axis), although the alignment appeared to return to the initial position. The change was probably due to transient phenomena associated with the progress of glue bonding. Therefore, we did not deal with it further. The change in the alignment before and after the second random vibration test, after the plate with a macro-slit was placed between the optics and CCD-PWB to reduce the stray light reflected from the CCD-PWB (re-integration), was within the measurement error.

This document is provided by JAXA.

Table 4-2 Measured alignment during the environmental tests

	-7°	0°	+7°
Azimuth direction (relative to the primary integration)			
After the vibration and shock tests[1] (QT, 3-axis)	47 μm	24 μm	3 μm
After the random vibration test[2] (AT, 1-axis)	20 μm	21 μm	17 μm
After re-integration[3]	32 μm	24 μm	15 μm
After the random vibration test[4] (AT, 3-axis)	20 μm	15 μm	8 μm
Elevation direction			
After primary integration[5]	55 pixels	1,334 pixels	2,529 pixels
After the vibration and shock tests (QT, 3-axis)	53 pixels	1,332 pixels	2,527 pixels
After the random vibration test (AT, 1-axis)	51 pixels	1,330 pixels	2,525 pixels
After re-integration	48 pixels	1,327 pixels	2,521 pixels
After the random vibration test (AT, 3-axis)	50 pixels	1,328 pixels	2,523 pixels

The alignment measurements were performed on [1] Jan. 7, [2] Jan. 12, [3] Feb. 10, [4] Feb. 19, 2004, and [5] Dec.23, 2003.

(2) MTF

The MTF was measured as follows. Images were taken of a chart containing a pattern of black and white stripes. The chart was moved at a speed that equaled the Nyquist frequency of LIC, i.e., 71.4 cycles/mm. Images of the white and black chart were taken separately. The *MTF* of a pixel was defined using the following equation.

$$MTF = \frac{DN_{\max}(MTF) - DN_{\min}(MTF)}{DN(white) - DN(black)}, \qquad \text{(Eq.4-2)}$$

where $DN_{max}(MTF)$, $DN_{min}(MTF)$, $DN(white)$, and $DN(black)$ are the maximum and minimum data numbers of the image of the stripe chart, and the data numbers of the white and black charts, respectively. A narrow band filter centered at 610 nm was used to examine the resolving power of LIC near the peak wavelength of the light reflected from the lunar surface. The intensity of the light source was adjusted by inserting a neutral density (ND) filter just before the LIC optics. The MTF was measured in both the elevation and azimuth directions. Figure 4-8 illustrates how the MTF is determined for the two orthogonal directions using horizontal (HMTF) and vertical (VMTF) stripe charts. The incidence angle of the collimator beam to the LIC optics was at 0, -7, and +7°. A vacuum-correction lens was equipped with the LIC optics and the lens temperature was kept at 30±3℃.

This document is provided by JAXA.

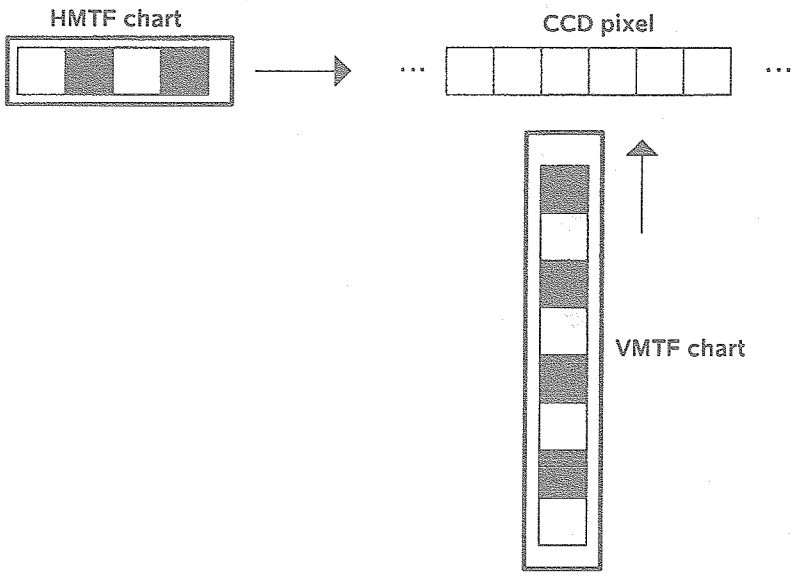

Figure 4-8 Orientation of the CCD array and the direction of the movements of the two orthogonal stripe charts for measuring the MTF in elevation (HMTF) and azimuth (VMTF) directions.

Figure 4-9 shows an example of the DN values of the chart images. The number of the sine wave differs in the two directions due to the use of a one-dimensional CCD. About forty maxima can be detected for the vertical (azimuth) direction, whereas only one or two maxima were obtained for the horizontal (elevation) direction. Accordingly, the measurement error of the HMTF is expected to exceed that of the VMTF. The values of the MTF measured at all gain modes agreed within ± 0.05 for the HMTF and ± 0.01 for the VMTF. The reproducibility of the measurements was within ± 0.04 and was typically within ± 0.01.

The MTF of the entire LIC system, including the optics and electronics, was evaluated before primary integration of LIC and was confirmed to be between 0.2 and 0.4 within the $\pm 7.3^{\circ}$ FOV. This value satisfies the specification (>0.1). After primary integration, the MTF was measured before and after the major environmental tests. The results are summarized in Table 4-3. As described in the previous section, the alignment was changed and the MTF value became lower than the required specification after a series of random vibration, point shock, and drop shock tests. However, further random vibration in one axis caused no further displacement of the defocus position or decrease in the MTF; therefore, we considered the displacement and decrease of the MTF to be transient phenomena associated with fixing of an adhesive. Accordingly, we did not change the fixing procedure or add new fixing points at re-integration. The fluctuation of the MTF values after re-integration is within or comparable to the measurement errors addressed above. The MTF values are better than the specified values.

This document is provided by JAXA.

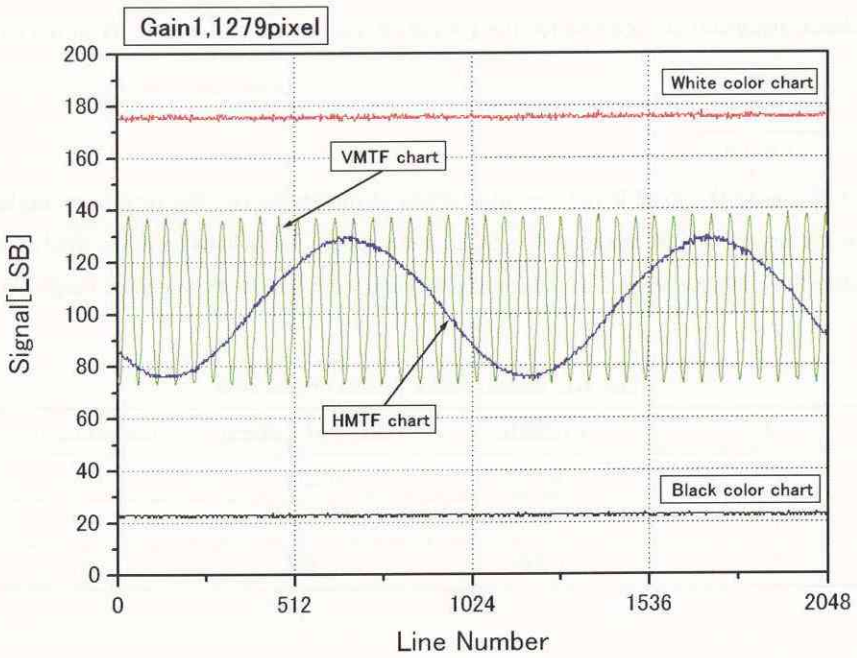

Figure 4-9 Profiles along a line of the images of the MTF measurements

Table 4-3 Measured MTF during the environmental tests

	49 pixels		50 pixels		1,279 pixels		1,280 pixels		2,509 pixels		2,510 pixels	
	H*1)	V*1)	H	V	H	V	H	V	H	V	H	V
After primary integration	—	—	0.27	0.43	—	—	0.33	0.43	—	—	0.32	0.31
After the vibration and shock test (QT, 3-axis)	—	—	0.21	0.22	—	—	0.19	0.13	—	—	0.06	0.07
After random vibration test (AT, 1-axis)	—	—	0.23	0.28	—	—	0.29	0.23	—	—	0.11	0.13
After re-integration	0.28	0.42	0.25	0.40	0.25	0.42	0.21	0.41	0.40	0.34	0.35	0.34
After the random vibration test (AT, 3-axis)	0.30	0.44	0.28	0.43	0.31	0.43	0.28	0.43	0.36	0.24	0.31	0.24
After the TV test	0.31	0.44	0.29	0.47	0.27	0.44	0.25	0.44	0.42	0.25	0.34	0.26

*1) H and V denote HMTF and VMTF, respectively.

This document is provided by JAXA.

(3) Distortion

Information about distortion is required for the geometric correction and was determined using the following equation.

$$Distortion = \frac{f \tan\theta - dY}{f \tan\theta}, \qquad \text{(Eq.4-3)}$$

where f, θ, d, and Y denote the focal length, rotation angle of the stage, i.e., the incidence angle, pixel pitch, and displacement of the rectangular chart image on the CCD, respectively. Table 4-4 shows the final measurement results for the distortion after the vibration tests. The values of distortion were within the specified range (less than 2%).

Table 4-4 Measurement results of distortion.

θ	Y (pixels)	f tan θ /d (pixels)	Distortion (%)
-7°	-1,238	-1,228	0.8
0	—	—	—
7°	1,235	1,228	0.6

(4) Linearity and gain factors

The trend of the responsivity of LIC was monitored throughout the environmental tests and the final pre-flight calibration data were obtained on March 15, 2004 after the TV test. A large integrating sphere (2 m diameter, 50 cm aperture), which was calibrated using a standard procedure at the National Research Laboratory of Metrology (e.g., Johnson et al. 1997), was used as a uniform, diffuse scattering light source. The radiance of the integration sphere was controlled by changing the number of lamps operating at a fixed voltage of 52±0.2 V. The lamp configuration is summarized in Table 4-5 and Figure 4-10. At the beginning of a test, twenty-four (24) lamps in the integration sphere were turned on for at least 1 hour before data acquisition, so that they would warm up. The radiance of the integration sphere was monitored at three wavelengths, 560, 660, and 810 nm, using power meters installed on the integration sphere. The stability of the radiance was within 1% during data acquisition.

This document is provided by JAXA.

Table 4-5 Configuration of the number of lamps on the integration sphere in the linearity test

Number of lamps	Lamps used	Gain0	Gain1	Gain2	Gain3
24	1, 2, 3, 4, 5, 6, 7, 9, 10, 11, 12, 13, 14, 15, 16, 17, 18, 19, 21, 22, 23, 24, 25, and 26	○			
16	2, 3, 5, 6, 8, 9, 11, 12, 15, 16, 18, 19, 21, 22, 24, and 25	○			
8	2, 5, 8, 11, 15, 18, 21, and 24	○	○		
6	4, 8, 12, 17, 21, and 25	○	○	○	
5	1, 6, 11, 16, and 21		○	○	○
4	1, 7, 14, and 21		○	○	○
3	1, 10, and 17			○	○
0(dark image)	—	○	○	○	○

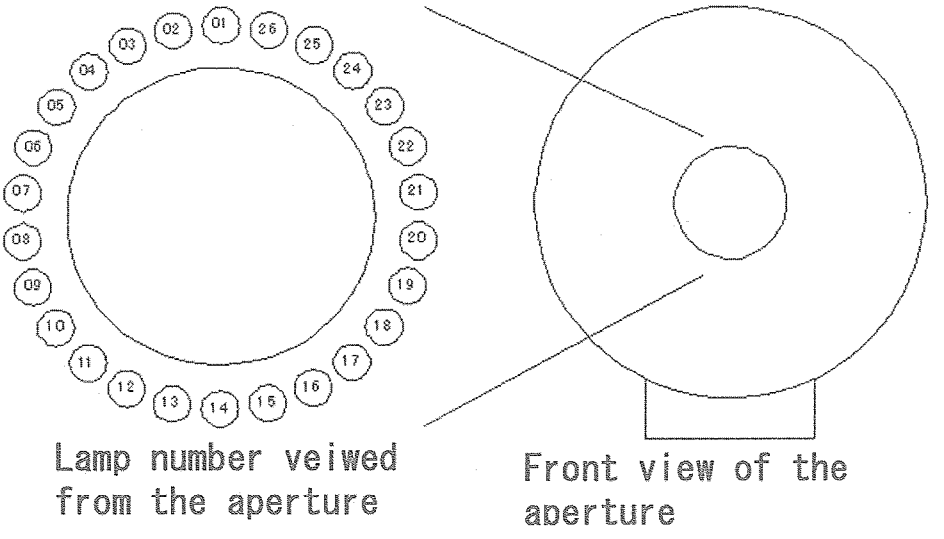

Figure 4-10 Configuration of the lamps of the integration sphere.

Images for the radiometric calibration tests were taken in the 1024 pixels×512 lines mode and all of the pixels of LIC were covered with three images by shifting the start pixel. The detector output was averaged through 512 lines, and subtracted with a dark image. Figure 4-11 shows the dark-subtracted average DN for pixels Nos. 1281 and 1282 at each gain mode as a function of the relative radiance measured by the power meter at 560 nm. The relative responsivity was estimated by line fitting for each gain. The maximum errors of the fitting throughout all pixels for Gain0, Gain1, Gain2, and Gain3 were 1.5, 1.0, 1.0, and 1.7%, respectively. These values met the specification of linearity (less than 5.0%). Table 4-6 shows the trend in the gain factors relative to Gain0 during the environmental tests. There were no apparent changes in the gain factors throughout the tests. To evaluate the effects of fluctuation of the power supply from the PCD, we carried out performance tests at three different voltages from the power supply to LIC. There was no detectable dependence of the gain factors on the voltage, within the measurement error.

This document is provided by JAXA.

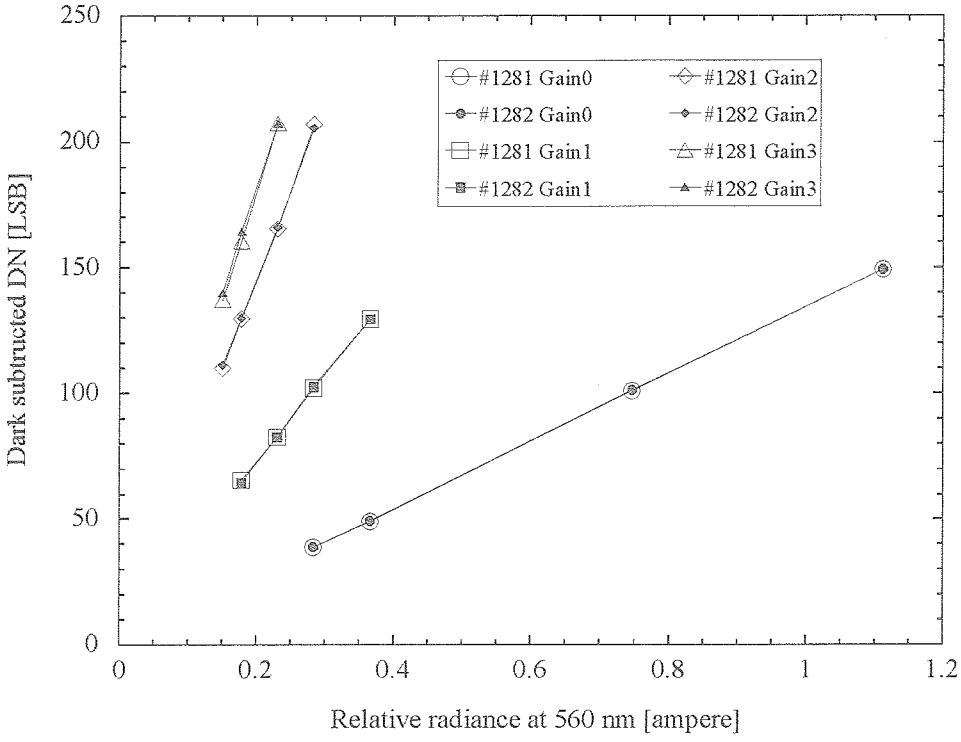

Figure 4-11 Dark-subtracted average DN for pixels Nos. 1281 and 1282 at each gain mode as a function of the relative radiance.

Table 4-6 Trend of the gain factors relative to Gain0 during the environmental tests

	Gain1/Gain0		Gain2/Gain0		Gain3/Gain0	
	1281 Pixel (Odd)	1282 Pixel (Even)	1281 Pixel (Odd)	1282 Pixel (Even)	1281 Pixel (Odd)	1282 Pixel (Even)
Design	2.67		5.34		6.67	
After primary integration	2.67	2.67	5.43	5.45	6.64	6.67
After the vibration and shock test (QT, 3-axis)	2.74	2.72	—	—	6.79	6.85
After re-integration	2.61 (-2.2%)	2.60 (-2.6%)	—	—	6.66 (-0.2%)	6.62 (-0.7%)
After the random vibration test (AT, 3-axis)	2.65 (-0.7%)	2.64 (-1.1%)	5.43 (0%)	5.43 (-0.4%)	6.62 (-0.3%)	6.65 (-0.3%)
After the TV test	2.67 (0.0%)	2.65 (-0.7%)	5.41 (-0.2%)	5.40 (-0.9%)	6.73 (1.4%)	6.79 (1.8%)

Fluctuations relative to the values after primary integration are shown in parentheses.

This document is provided by JAXA.

(5) Flatfield

Profiles of the relative responsivity, i.e., the flatfield, are shown in Figure 4-12. The decreasing responsivity of the optical vignetting at both ends of the elevation was less than 30%, which meets the specifications. There was a wavy pattern in the flatfield profile, especially at the middle of the pixels. The positions of the peaks in the waves are the same in the images of the integration sphere with two narrow band-path filters of 450 and 650 nm, as shown in Figure 4-13, and they are also consistent with the pattern of the responsivity of the CCD sensor itself, as shown in Figure 4-14. Note that the convex shape of the responsivity in Figs. 4-12 and 4-13 are due to the vignetting, while the responsivity curve shown in Fig.4-14 was obtained without the lens-system. Accordingly, the wavy pattern is not an interference fringe, but is due to the non-uniformity of the sensitivity of the detector photo-diodes.

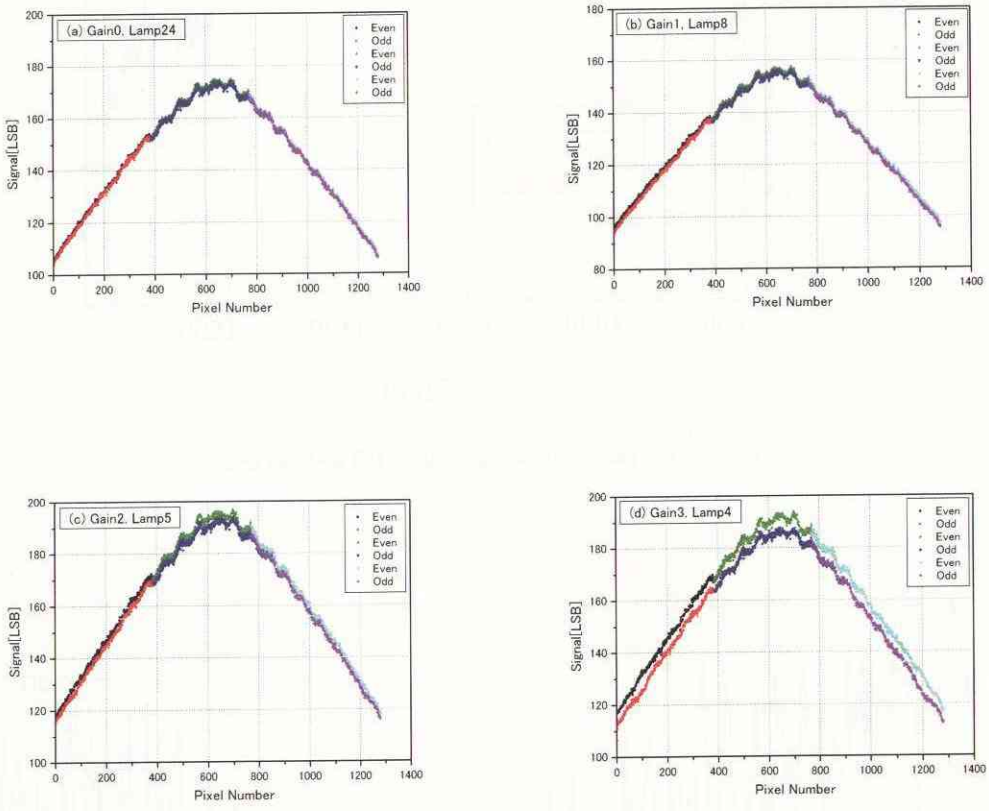

Figure 4-12 Average responsivity of all of the pixels at each gain. (a) Gain 0 and (b) Gain1, (c) Gain2 and (d) Gain3.

This document is provided by JAXA.

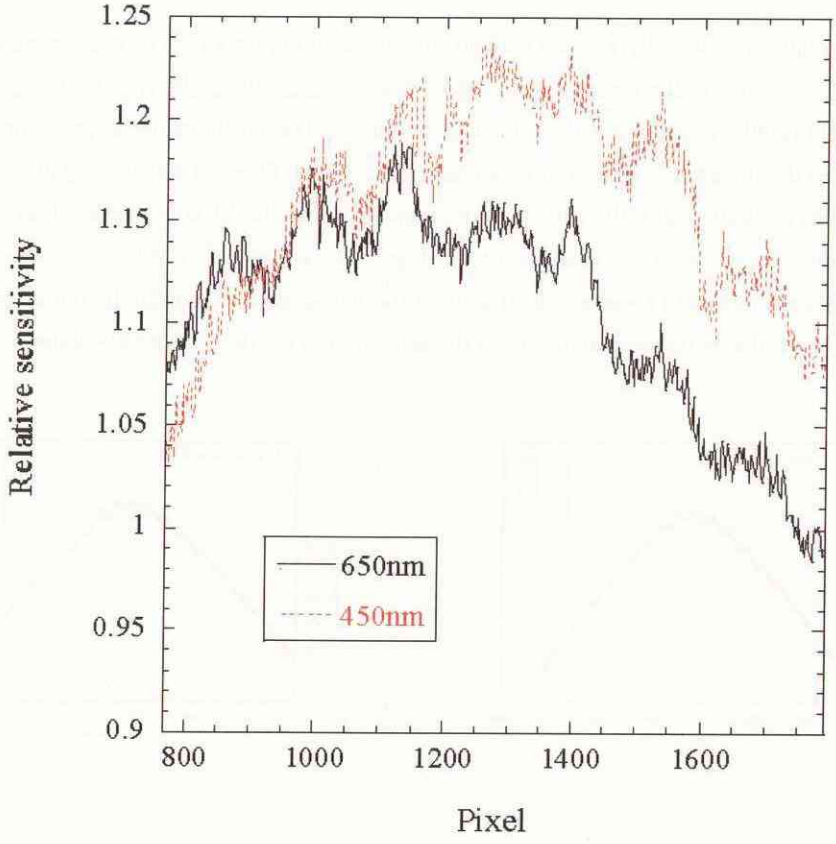

Figure 4-13 Narrow band flatfields at 450 and 650 nm.

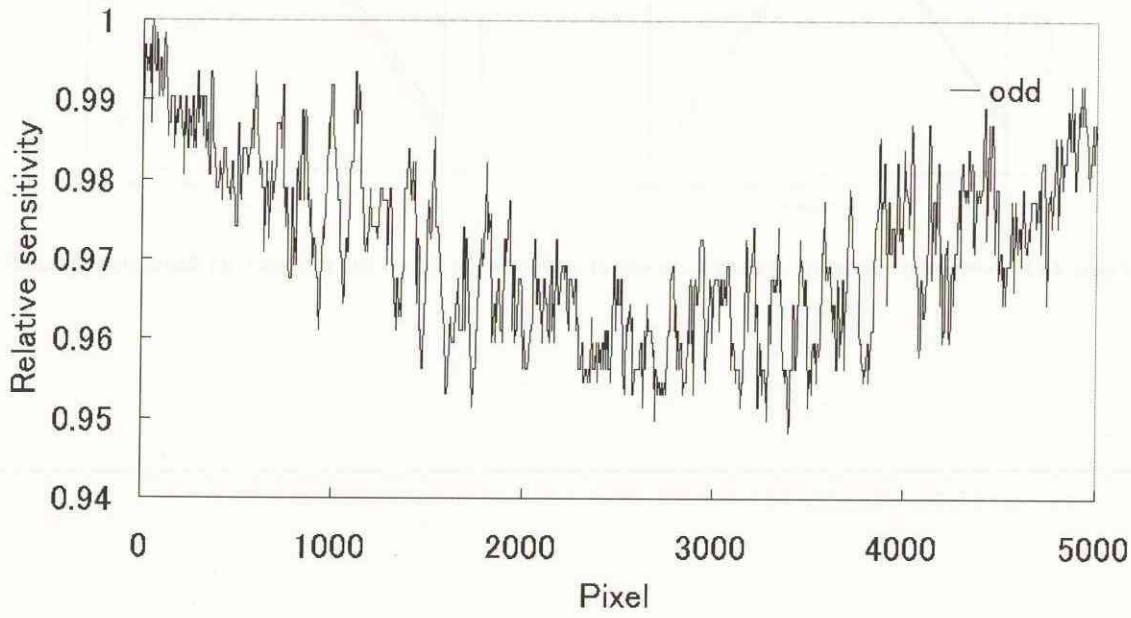

Figure 4-14 Relative sensitivity of the photo-diodes of the LIC CCD sensor. Only odd pixels are shown. LIC uses pixels between the first and the 2560-th.

This document is provided by JAXA.

(6) Absolute responsivity

The equation describing the relationship between the raw digital number, DN (LSB), and the physical units of radiance is:

$$DN_{Gain,Pixel} = A_{Gain,Pixel} \int \frac{\pi \cdot t}{4F^2} J(\lambda) \cdot f(\lambda) d\lambda + Dark_{Gain,Pixel}, \quad \text{(Eq.4-4)}$$

where $DN_{Gain,Pixel}$ is the raw digital number at the specified pixel and the specified gain; F is the F-number of the optics; t is the integration time; $J(\lambda)$ is the spectral radiance of the light source; $f(\lambda)$ is the spectral responsivity of the LIC CCD sensor and the optics; $Dark_{Gain,Pixel}$ is the dark level; and $A_{Gain,Pixel}$ is the responsivity. $f(\lambda)$ is assumed to be the product of the system spectral responsivity of LIC (Figure 3-4). $A_{Gain,Pixel}$ is a product of the gain, the analog-digital conversion ratio, and the flatfield. Once $J(\lambda)$ of the integration sphere is supplied, $A_{Gain,Pixel}$ can be estimated. Figure 4-15 shows a measured $J(\lambda)$ of the integration sphere in eight-lamp mode at an operating voltage of 52 V. The derived $A_{Gain,Pixel}$ is shown in Figure 4-16.

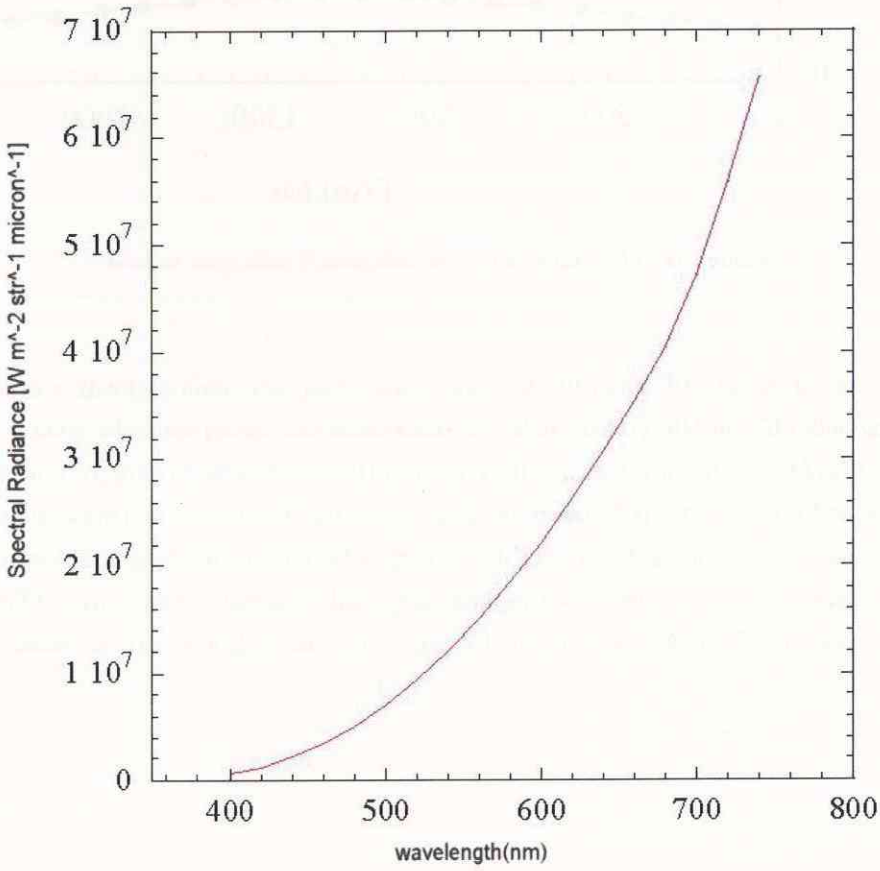

Figure 4-15 Absolute calibration value of the integration sphere. Eight lamps were turned on.

This document is provided by JAXA.

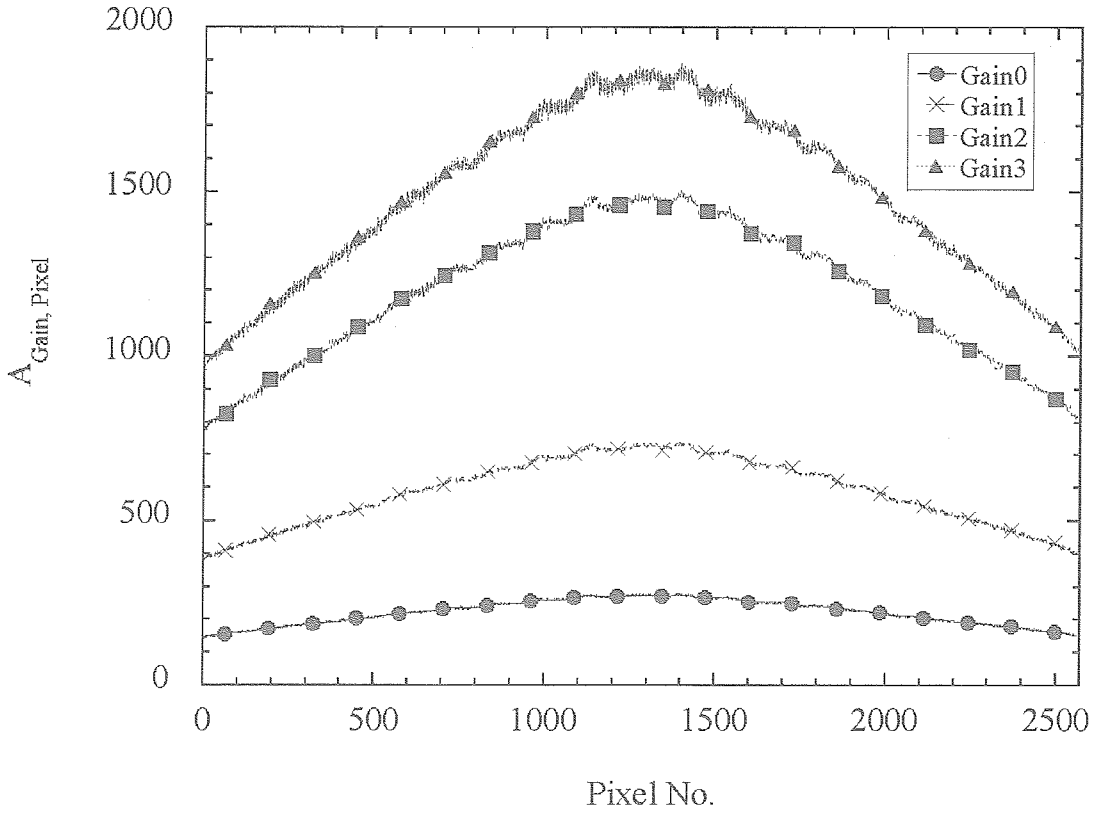

Figure 4-16 Absolute sensitivity of each pixel at each gain, $A_{Gain,Pixel}$.

The above procedure for estimating the absolute responsivity was confirmed with a ground-based lunar observation using both LIC and MIC proto-models. The observation was carried out under a full moon, at which the phase angle is~0° and the spatial distribution of the radiance of the moon depends mostly on the distribution of the surface materials and their spectral reflectance. In other words, the illumination and viewing geometries can be neglected. Figure 4-17 shows an image taken using the proto-model of LIC. A (spectral average) geometric albedo of a dark region of the moon was inferred from the DN of the image and the absolute responsivity of LIC after correcting for atmospheric absorption. The estimated albedo of 0.08 is in accordance with previous observations.

This document is provided by JAXA.

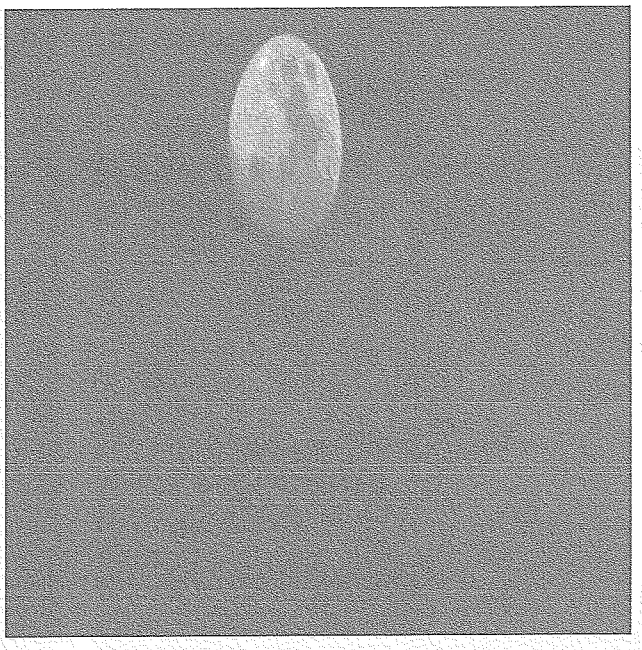

Figure 4-17 Image of the moon taken from the ground on November 22, 1996. Gain1, image size 512×512. The scan direction is vertical in the image. The aspect ratio of the image was not corrected.

(7) Two-dimensional imaging

As one final check of the subsystem, the flight model of LIC took a two-dimensional image to check the polarity using the collimator. A chart of an aerial photograph was moved in the azimuth direction, simulating the spin motion of the spacecraft. Figure 4-18 compares the original image copied using a digital camera ("chart map") and the raw LIC image. The size of the chart on the LIC image in the elevation direction was 148 pixels. Since the moving speed of the chart varied, we processed the LIC image as follows. First, the chart map was rotated by 0.52° after comparing the position of corresponding features on the chart map and LIC image. Next, the corresponding part of the chart map was binned into 148 pixels in the horizontal direction to make the horizontal resolution the same as that of the LIC image. Then, each line of the LIC image was compared with one line of the chart map. A corresponding line on the chart map for a given line in the LIC image was selected by maximizing the correlation coefficient. Figure 4-19 shows the correlation coefficient for each of the lines in the LIC image. The local peaks of the correlation coefficient indicate the central lines in the LIC image that correspond to the lines of the chart map. The widths of the peaks are in relation with the moving speed of the chart. The moving speed was slowed for the lower lines in the LIC images as shown in Fig. 4-18. Finally, we resized the LIC image in the azimuth direction and obtained the image in Figure 4-18. The resolution-corrected chart map is also shown. Therefore, the polarity of the LIC imaging was confirmed and the spatial resolution of the LIC image was confirmed qualitatively by looking at the special features in the chart map that were resolved in the LIC image.

This document is provided by JAXA.

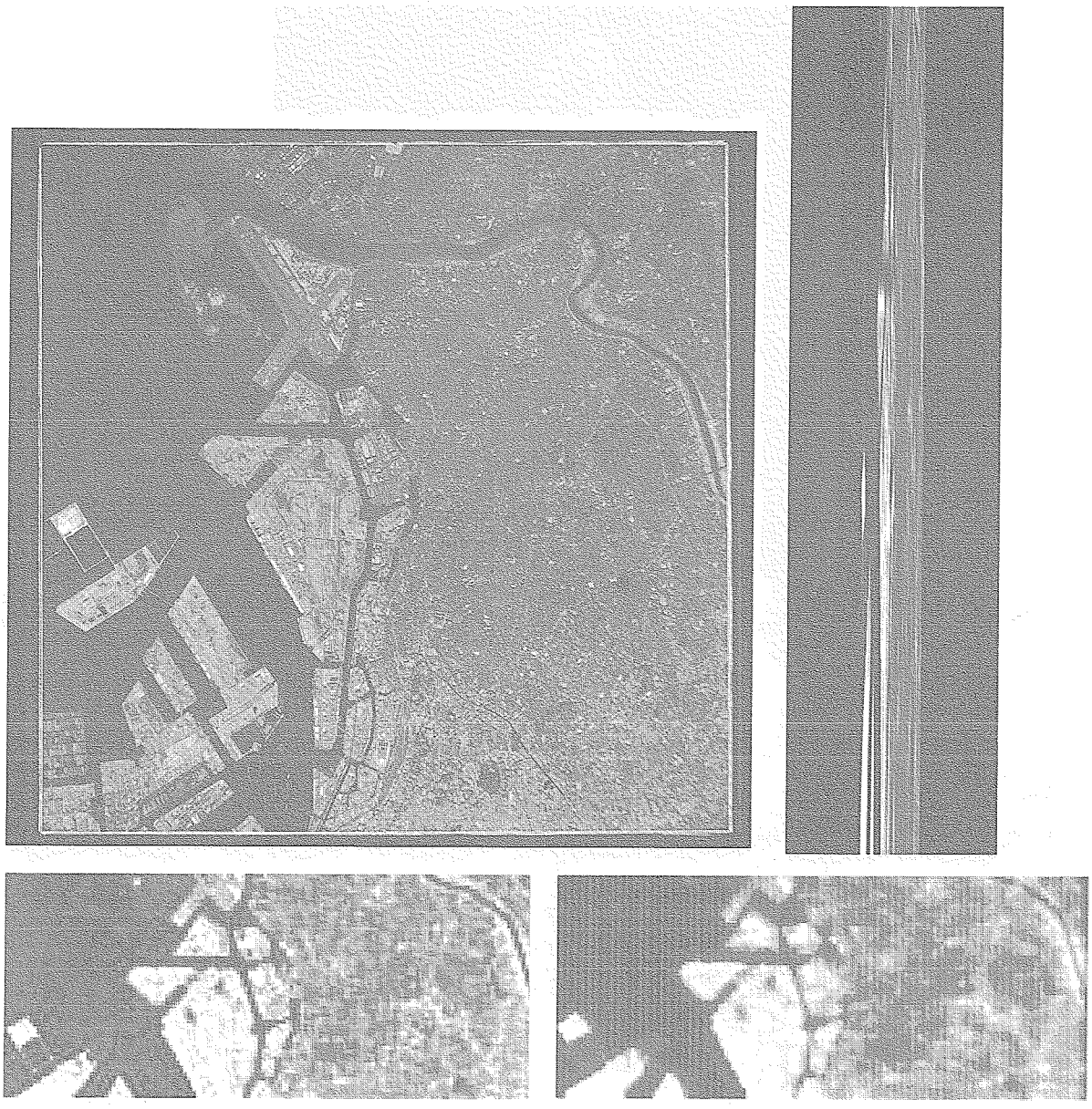

Figure 4-18 A comparison of the original chart image (upper left) and the raw 512×2048 LIC image (upper right). The chart image is an aerial photo of Haneda airport. The lower left is the resolution-corrected chart map. The lower right is the resized LIC image.

This document is provided by JAXA.

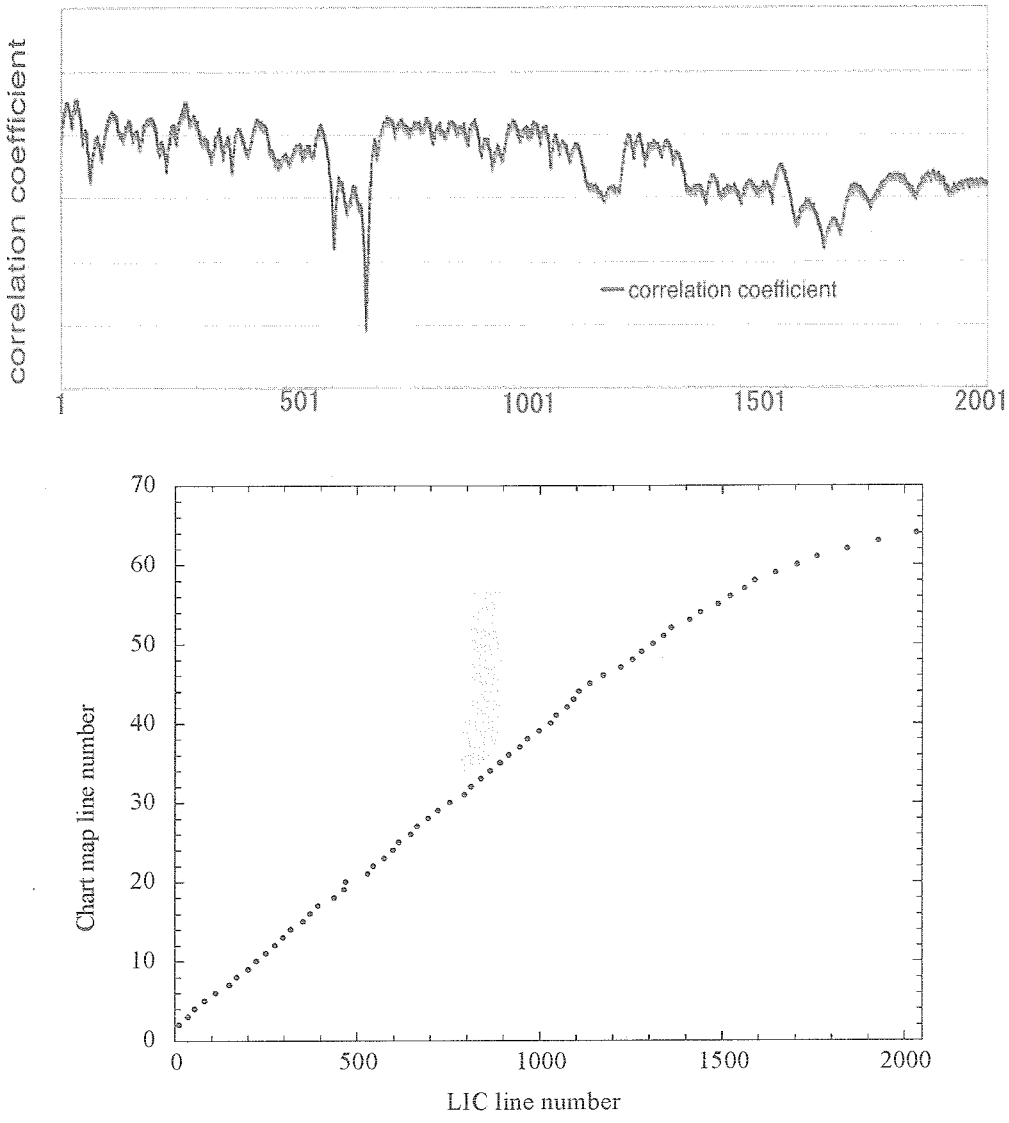

Figure 4-19 The correlation coefficient of the lines (upper) and the correspondence of the lines in the LIC image and the chart map (lower).

(8) Estimating stray light

LIC has no hood, but the solar paddles restrict direct irradiation from the Sun. However, solar light reflected from the lunar surface outside the FOV of LIC can be a source of stray light. The structure of the solar paddles mainly consists of a deployment mechanism and a substrate. The substrate mounting solar cell arrays is made of honeycomb sandwich panel with CFRP face sheets and is reinforced with CFRP stiffeners. Its dimensions are 981 mm×1044 mm, and 10 mm in thickness (see Figure 4-22). The surface of the CFRP face sheets is not finished with a highly absorbent black finish, however, the reflectance is very low (a measurement at our laboratory showed that the bi-directional reflectance at i=30, e=0, g=30 condition was less than 1.5%). Therefore, there is no possibility that the reflected light from the reverse side of substrate will become a secondary source of stray light. In nominal operation, LIC points toward lunar surface areas near the terminator. This imaging geometry allows the bright lunar surface to be next to the FOV of the LIC optics. We examined the effect of light from outside the FOV by taking images of the integration

This document is provided by JAXA.

sphere using a cylindrical hood. Figure 4-20 illustrates the test configuration.

The results are shown in Figure 4-21. The DN values were about 2% lower with the hood than without the hood at both Gain1 and Gain3, possibly owing to stray light from outside the FOV. In other words, the level of the stray light from outside the FOV was comparable to or less than the other uncertainties in the DN values due to other sources, such as electrical noise and compression error. Since the intensity of the integration sphere was stable within 1%, the other possible reason for the results is fluctuation in the dark level.

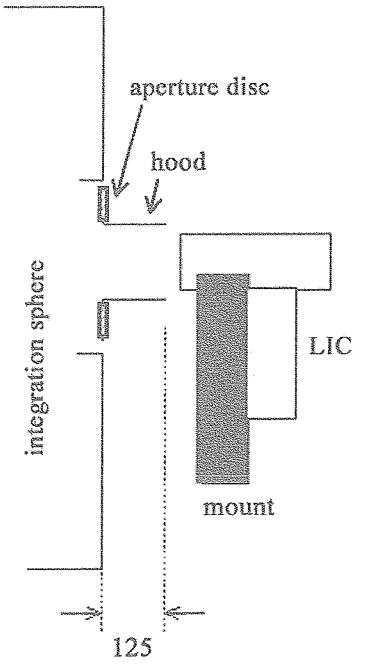

Figure 4-20 Configuration of the imaging with cylindrical hood.

This document is provided by JAXA.

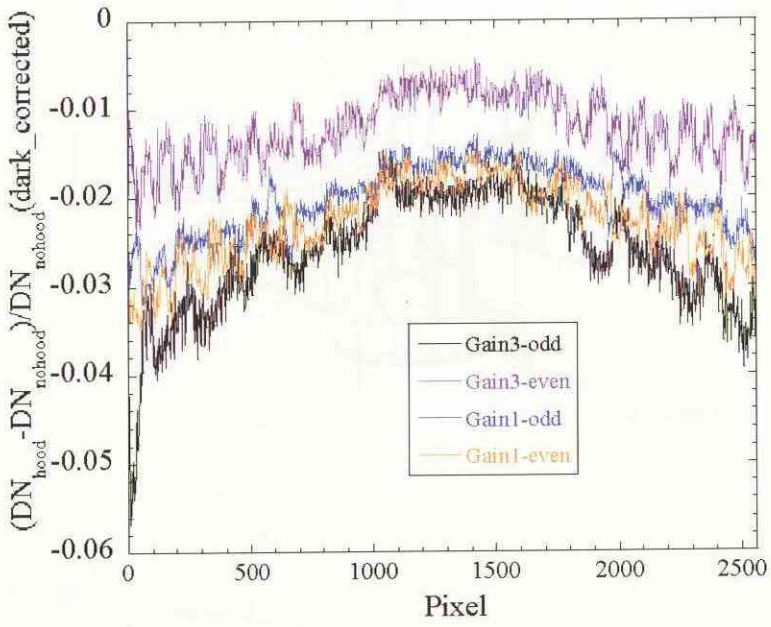

Figure 4-21 Comparison of flatfields taken with and without the hood. The images were taken in Gain1 or Gain3 modes with eight or five lamps in the integration sphere.

4. 3. MECHANICAL ENVIRONMENTAL TESTS

(1) Structure of LIC and mechanical environmental condition

First, we outline the structure of LIC and its installation on the spacecraft and then we describe the test conditions. The side of the orbiter is equipped with four "instrument boxes" placed symmetrically to each other with respect to the spin axis. Each instrument box consists of a front panel (the panel furthest from the spin axis) and four others. The panels are made of aluminum honeycomb. Figure 4-22 illustrates the configuration of the components of the orbiter. LIC will be installed inside one of the instrument boxes, attached to the front panel (called the "access panel"). The access panel has a circular window for the LIC optics. The optical axis of LIC is orthogonal to the spin axis. The LIC optics have no hood or access panel, either, to meet the weight restriction: however, a damper plate was inserted between the access panel and the installation surface of LIC. Figure 4-23 shows the dimensions and coordinate system of LIC and Table 4-7 summarizes the values of the moment of inertia of LIC. The total weight of LIC is 2448g.

The conditions of the mechanical environmental tests of LIC were based on a numerical simulation of the entire orbiter system and the results of environmental tests of a mechanical test model. Table 4-8 and Figure 4-24 show the test conditions. The resonance frequency of the LIC body exceeds 600 Hz, whereas the vibration level at frequencies of 600-800 Hz is estimated to be 0.12 - $0.2G^2$/Hz and is within the tolerance limits of the LIC body against vibration along each axis. Table 4-9 shows the test flow and items.

This document is provided by JAXA.

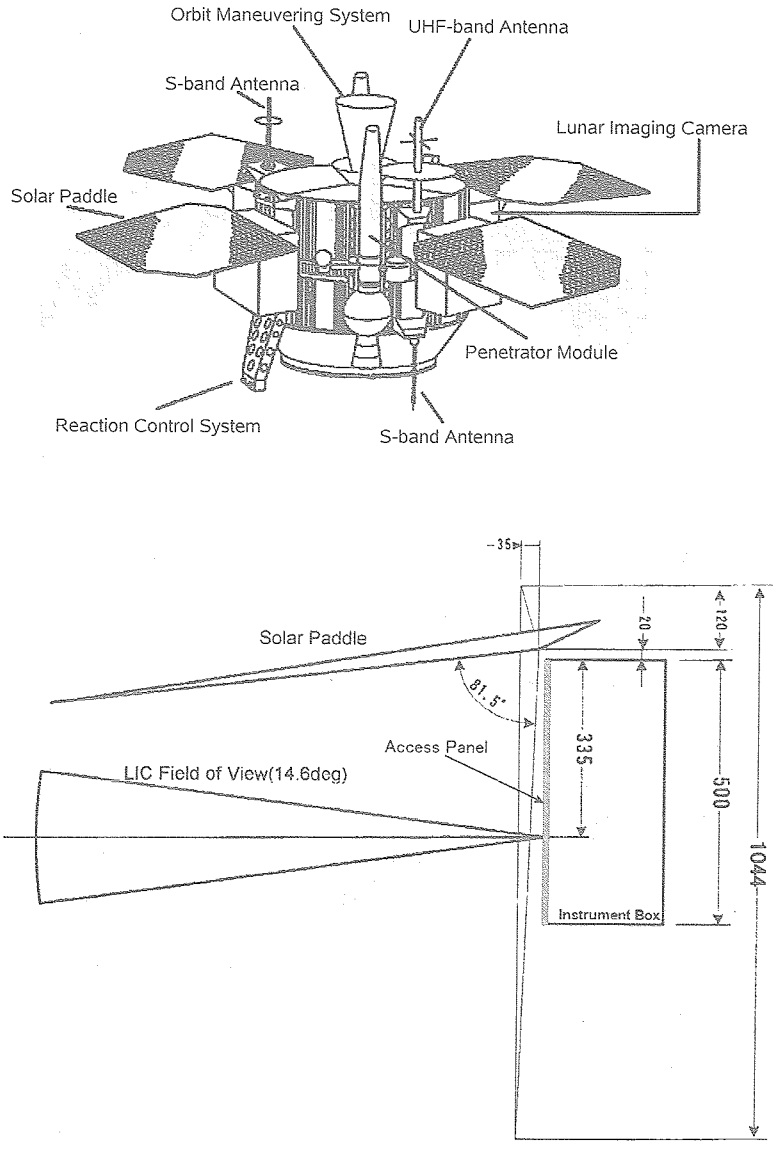

Figure 4-22 Configuration of the LUNAR-A orbiter (upper) and relative location of the solar paddle and the FOV of the LIC optics (lower). The rear side of the paddle is made of CFRP and has low reflectivity.

This document is provided by JAXA.

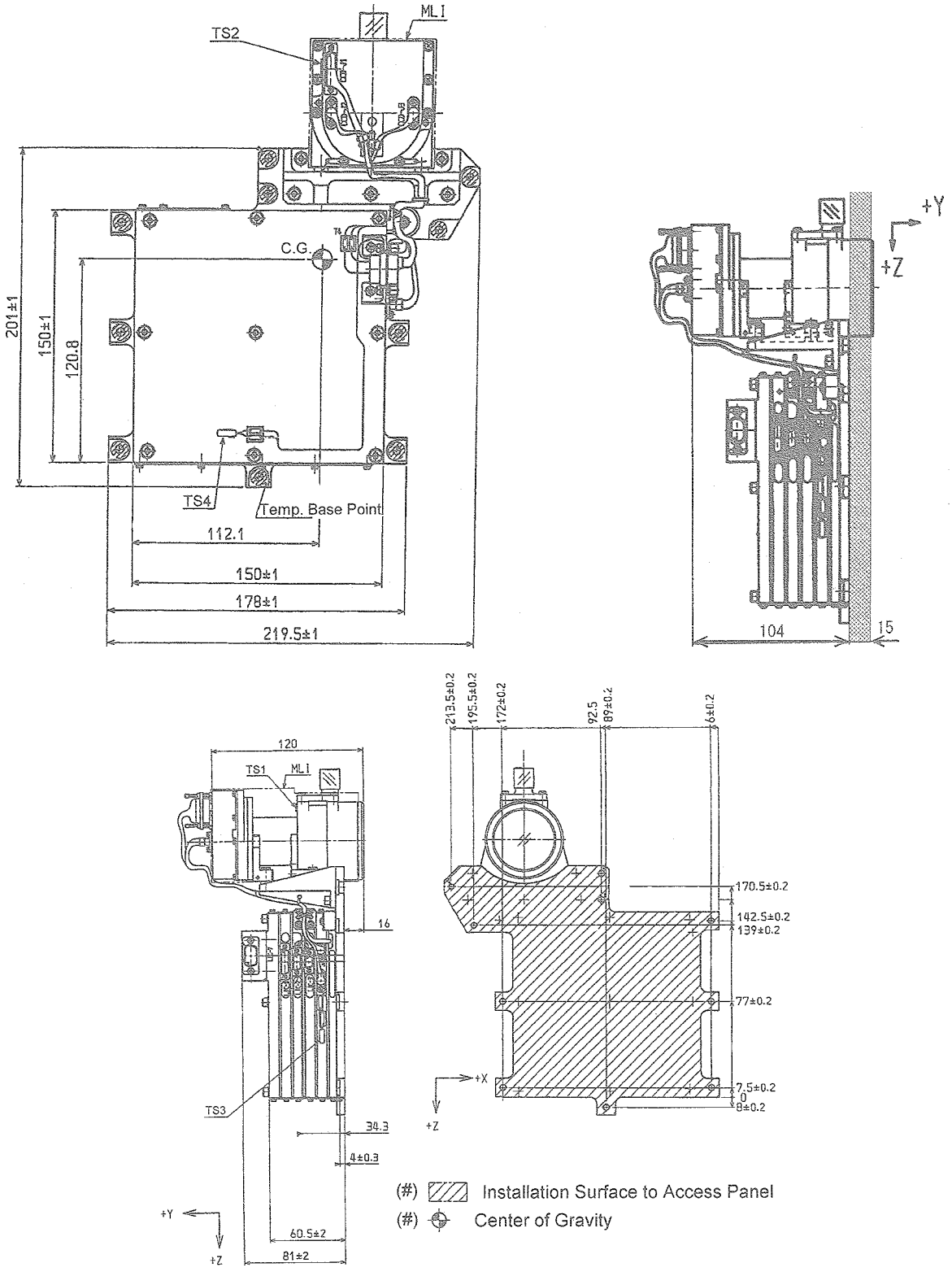

Figure 4-23 Dimensions of LIC and coordinate system. The numbers are scales in mm. TS1 to TS4 represent the locations of platinum thermometers. The upper right figure illustrates the configuration of the acces panel by the shadow.

This document is provided by JAXA.

Table 4-7 Moment of inertia of LIC

Moment of inertia*1)	Value (kg cm²)
Ix	71.6
Iy	71.5
Iz	141.1

*1) Ix, Iy, and Iz are the moment of inertia around the x, y, and z-axes, respectively. The coordinate system is defined in Fig. 4-23.

Table 4-8 The condition of the vibration and shock tests.

Test item	Level	Level accuracy	Time duration
Random vibration test	Shown in Figure 4-24	0 - +3 dB	50 s
Drop shock test	+25 G (horizontal) +15 G (vertical)	Within 15% of the peak G	10 ms (half sine wave)
Point shock test	+8 dB/octave (10-1000Hz) 500G srs*1) (1000-4000Hz)	SRS*1) +50%, -10%	—

*1) SRS is an abbreviation for the shock response spectrum. The SRS reflects the maximum absolute acceleration of a single degree of freedom excited at the base by the transient acceleration representing the short-period shock. The calculation procedure of SRS is discussed in detail in Wijker (2004).

This document is provided by JAXA.

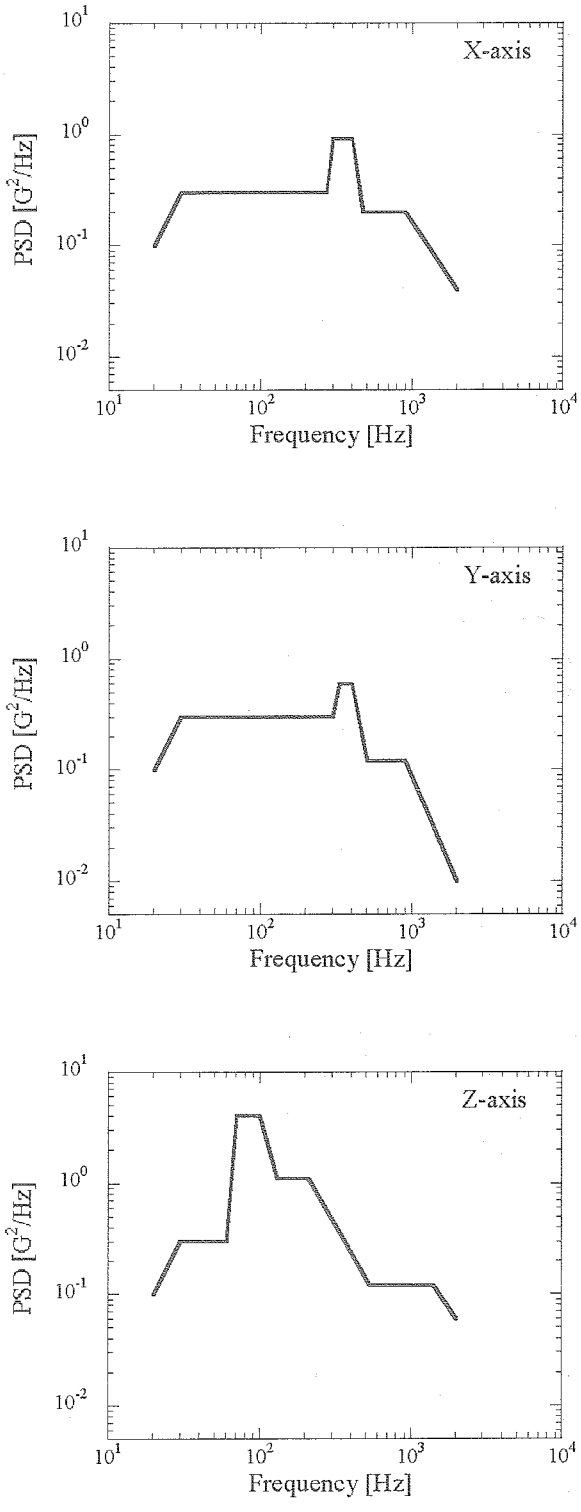

Figure 4-24 Conditions for the power spectral density (PSD) of the random vibration test along the x, y, and z-axes.

This document is provided by JAXA.

Table 4-9 Test flow and items.

Test	Test item	Status of LIC
Set-up for the random vibration test		
Random vibration test	1. Power consumption measurement and dark image acquisition	CCD driven
	2. Object image acquisition (imaging fluorescent light)	
	3. Low level vibration test along the Y-axis	LIC off
	4. Examination from outside of the LIC body	LIC on (power is supplied to electronic circuit, but the CCD is off)
	5. QT level vibration test along the Y-axis	
	6. Examination from outside of the LIC body	CCD driven
	7. Power consumption measurement and dark image acquisition	
	8. Low level vibration test along the Z-axis	LIC off
	9. Examination from outside of the LIC body	
	10. QT level vibration test along the Z-axis	LIC on
	11. Examination from outside of the LIC body	
	12. Power consumption measurement and dark image acquisition	CCD driven
	13. Low level vibration test along the X-axis	LIC off
	14. Examination from outside of the LIC body	
	15. QT level vibration test along the X-axis	LIC on
	16. Examination from outside of the LIC body	
	17. Power consumption measurement and dark image acquisition	CCD driven
	18. Object image acquisition	
Set-up for drop shock test		
Drop shock test	1. Drop shock test along the X+ direction	LIC off
	2. Drop shock test along the X+ direction	
	3. Drop shock test along the Y+ direction	
	4. Drop shock test along the Y+ direction	
	5. Drop shock test along the Z+ direction	
	6. Drop shock test along the Z+ direction	
	7. Dark image acquisition	CCD driven
	8. Object image acquisition	
Set-up for point shock test		
Point shock test	1. Point shock given along the X-axis	LIC off
	2. Point shock given along the Y-axis	
	3. Point shock given along the Z-axis	
	4. Dark image acquisition	CCD driven
	5. Object image acquisition	

This document is provided by JAXA.

(2) Results of the mechanical environmental tests

First, the random vibration test was conducted at half of the required levels to ensure that the vibration does not result in resonance vibration. Then the QT level test was carried out for each axis and the performance of LIC before and after the test was compared. Table 4-10 summarizes the load conditions of the low level and QT level vibration test and the results. Although the offset level varied between the dark images taken before and after the test on each axis (Figure 4-4), the rest of the mechanical environmental tests were conducted, because the power consumption and values of the HK telemetry items did not change, and the imaging operation just after each vibration test was completed normally. The change in the offset level was probably caused by a change in either (a) ground state of the LIC electronics by the vibration, (b) the temperature of the LIC electronics or non-uniformity in temperature, or (c) the ground state due to any environmental condition in the test room. The imaging operation was completed normally before and after the point shock and drop shock tests, too.

Table 4-10 Measured acceleration levels in the random vibration test.

Test	Axis of vibration	Specification (within 10% of the value below)	Total measured Grms	
			LIC	Mount
Low level test (half the QT level test)	X	9.95	9.16 (92%)	9.55
	Y	8.0	7.74 (97%)	8.14
	Z	13.0	13.94 (107%)	13.22
QT level test	X	19.9	21.39 (107%)	20.04
	Y	16.0	—(profile was not taken)	16.20
	Z	26.0	28.25 (109%)	25.77

(3) Results of the optical performance test after the mechanical environmental tests

After finishing all of the mechanical environmental tests, we examined whether the LIC performance differed from that before the environmental tests. The items tested were the linearity, gain factors, MTF, and the alignment of the lens-system and CCD. There was no significant change in the linearity or gain factors (Table 4-6), whereas the MTF and alignment changed (Tables 4-2 and 4-3). The details are described in section 4-2.

The LIC performance was tested after re-integration and the second random vibration test. The changes in MTF and alignment were within the measurement error and specifications.

4. 4. THERMAL VACUUM TEST

(1) Thermal model of LIC and in-flight thermal conditions

The temperature conditions and thermal characteristics of LIC are summarized in Table 4-11. A numerical analysis using a thermal mathematical model (TMM) was performed and the flight temperature profiles of the LIC components were predicted. The TMM subdivides the thermal system into a number of finite sub-volumes called nodes. The thermal properties of each node are considered concentrated at the central nodal point of each sub-volume. The TMM of LIC has fifteen (15) nodes, as illustrated in Figure 4-25. Table 4-12 shows the results of the analysis. The temperature of the electronic circuit was maintained within the range from room temperature to 40℃, mainly by the heat input from the installation surface for the access panel and its own heat dissipation. The temperature of the lens-system was controlled to 30±3℃ by a sheet-shaped thin heater attached to the tube

This document is provided by JAXA.

framework for the lens-system.

(2) Thermal vacuum test

The thermal vacuum (TV) test was carried out in order to (a) perform baking within the storage temperature and confirm the thermal tolerance of LIC, (b) examine the imaging performance and function within the operational temperature range, and (c) verify the TMM through thermal balance tests.

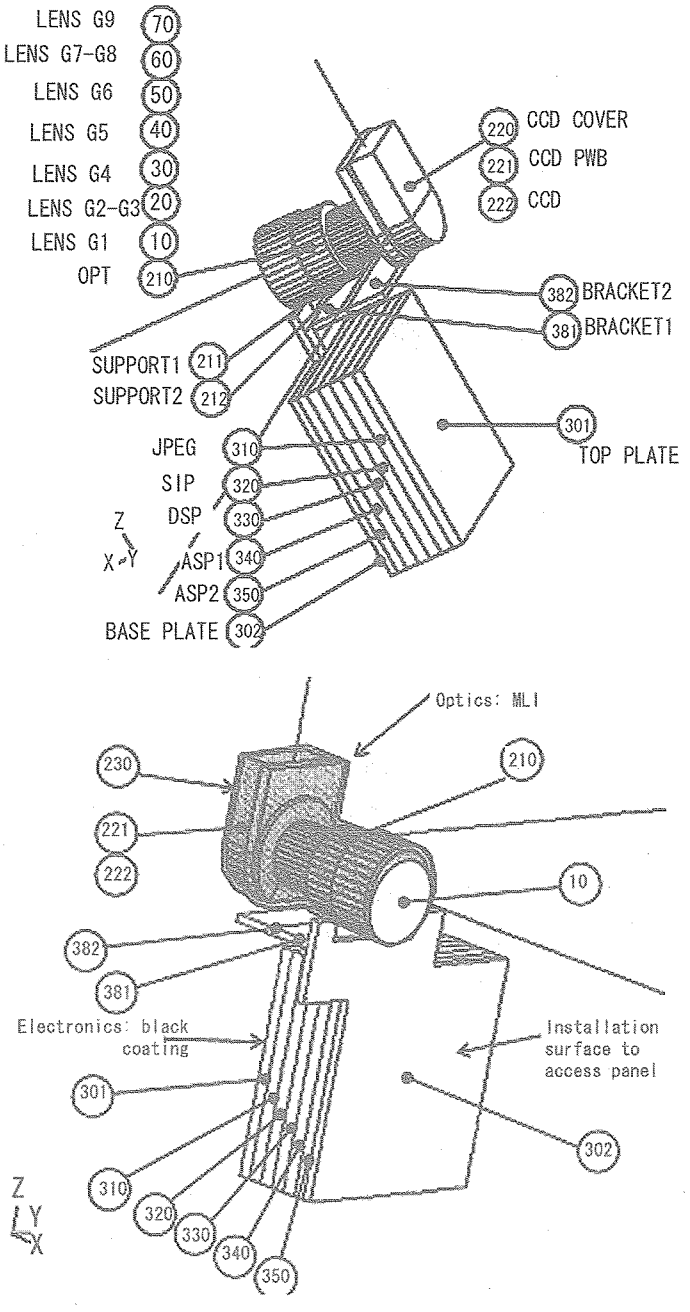

Figure 4-25 Nodes in the TMM of LIC.

This document is provided by JAXA.

Table 4-11 Thermal conditions and specifications of LIC

Items	Specifications
Temperature condition	
Operating temperature range	Electrical circuit: - 25 - + 40℃ Optics: +27 - + 33℃
Storage temperature range	- 40 - + 50℃
Turning on/off temperature range	- 25 - + 40℃
Surface treatment	
Installation surface	Electroless nickel plating
Outer surface	CCD-ASSY: Multilayer insulator blanket (MLI) Electronic box: black paint Surface of the optics: glass (radiation hardened)
Thermo-optic properties of outer surface	
Infrared absorption efficiency	MLI: 0.05 Black paint: 0.8 Glass: 0.80
Sunlight absorption efficiency	Glass: 1.0
Heat capacitance *1)	2097±80 J℃
Heat dissipation at each operating mode	
LIC on	3.3±0.5 W
CPU reset *2)	2.7±0.5 W
CPU run	3.5±0.5 W
CCD on	5.6±0.5 W
CCD driven	9.3±0.8 W
HTR on	3.6±3.0 W

*1) Measured value in the sub-system TV test.
*2) A mode in which electricity is supplied to the CPU, but the status of the CPU is idle.

Table 4-12 Flight temperature prediction for each component of LIC based on a thermal analysis.

Components		During the data relay orbit, when CCD is turned on (℃) *1)	During the trans-lunar orbit, when CCD is turned off (℃)
Electronics	Case	24.0 - 32.1	14.1 - 24.3
	Bracket	27.9 - 29.2	26.6 - 28.1
Optics	Support	28.4 - 30.0	27.8 - 29.5
	CCD	31.2 - 38.6	27.1 - 34.1
	Lens	29.0 - 31.0	29.0 - 30.9

*1) The temperature will converge on these values during imaging operations every revolution around the Moon.

The electrical connection diagram for the TV test and the test configuration of LIC and infrared (IR) panels in a vacuum chamber are shown in Figures 4-26 and 4-27, respectively. LIC was attached to a temperature-controlled plate that was placed in the chamber through a base plate and surrounded by four IR panels measuring 500×284 mm. The IR panels were attached to sheet-heaters to control the LIC and its surroundings to be nearly isothermal during the thermal balance tests. The relatively small room separated by the IR panels prevented the LIC unit from resulting in

This document is provided by JAXA.

large thermal gradients and a high temperature transition rate. In addition, to evaluate the thermal mathematical model of LIC, both the temperature data of IR panels and heat input values are used as boundary conditions of the external thermal interface, and therefore, they can simplify the model analysis. The mount measuring 315×270mm used in the test was the same one used in the electrical and optical performance tests simulating the access panel of the instrument box of the orbiter. The temperature of the temperature-controlled plate was varied between -40 and +50℃. The sheet-shaped thin heaters with an electric resistance of 100 and 43 ohms, respectively, were attached to the mount of the LIC and two 12-ohm sheet heaters were attached to each of the IR panels. The optics of LIC viewed the interior of a shroud in the chamber through the window of the mount. The temperature of the shroud was kept at -173℃, simulating interplanetary space. During the object imaging operation, LIC was illuminated by a fiber light source from the front of the window.

The planned temperature profiles of the LIC electronics and optics during the test are illustrated in Figure 4-28. The TMM was verified using temperature data at each node and the amount of heating for the optics taken at thermal equilibrium temperatures of -25, +30, and 40℃. Thermocouples were attached to the points in the LIC components listed in Table 4-13. The temperature base points, that are interface (I/F) points, are located on the installation surface of the access panel where the heat flux under flight condition is defined. The model simulating the TV test included additional nodes for the mount, IR panels, base plate, and shroud. The imaging function and performance were verified at the thermal equilibria mentioned above. The power supply to LIC was turned off at temperatures exceeding the operating range (+50 and -40℃).

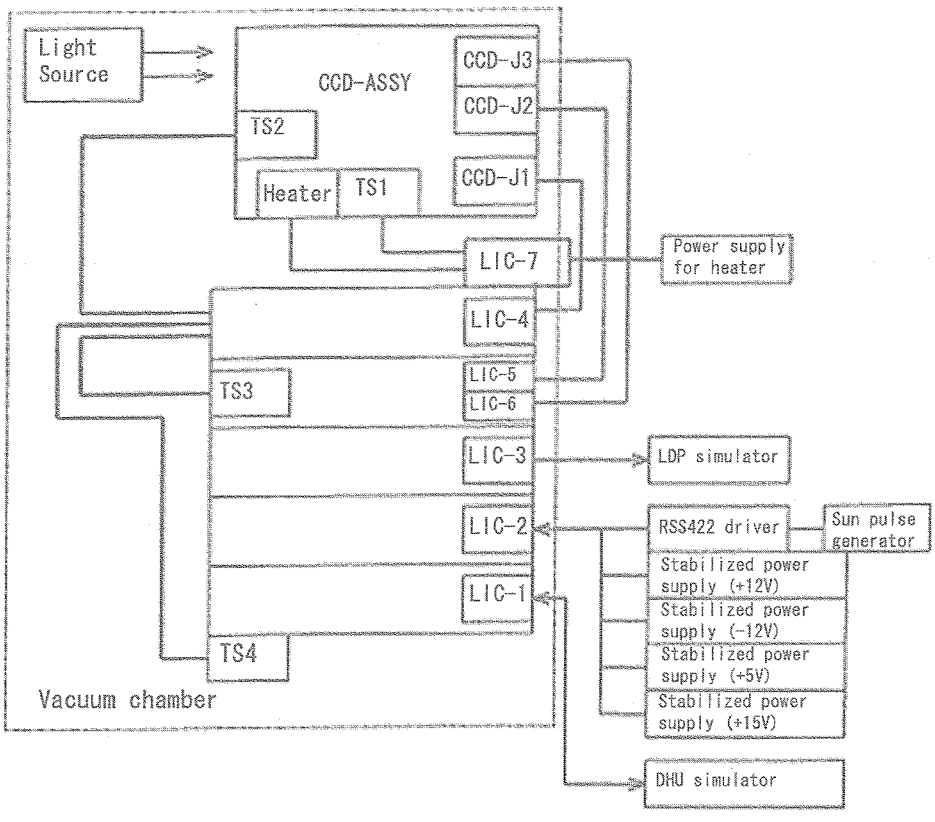

Figure 4-26 Electric connection diagram for the TV test.

This document is provided by JAXA.

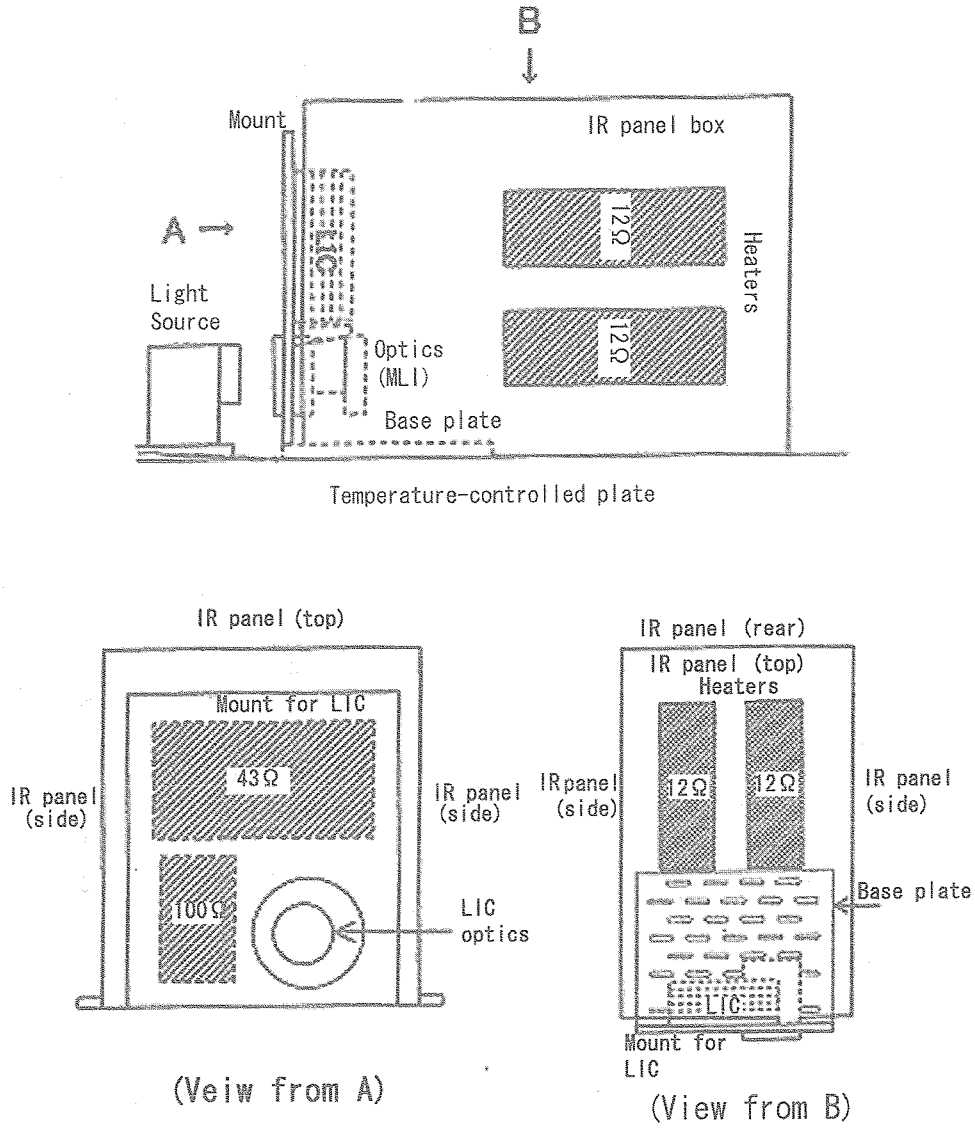

Figure 4-27 Configuration of LIC and the IR panels in the vacuum chamber.

This document is provided by JAXA.

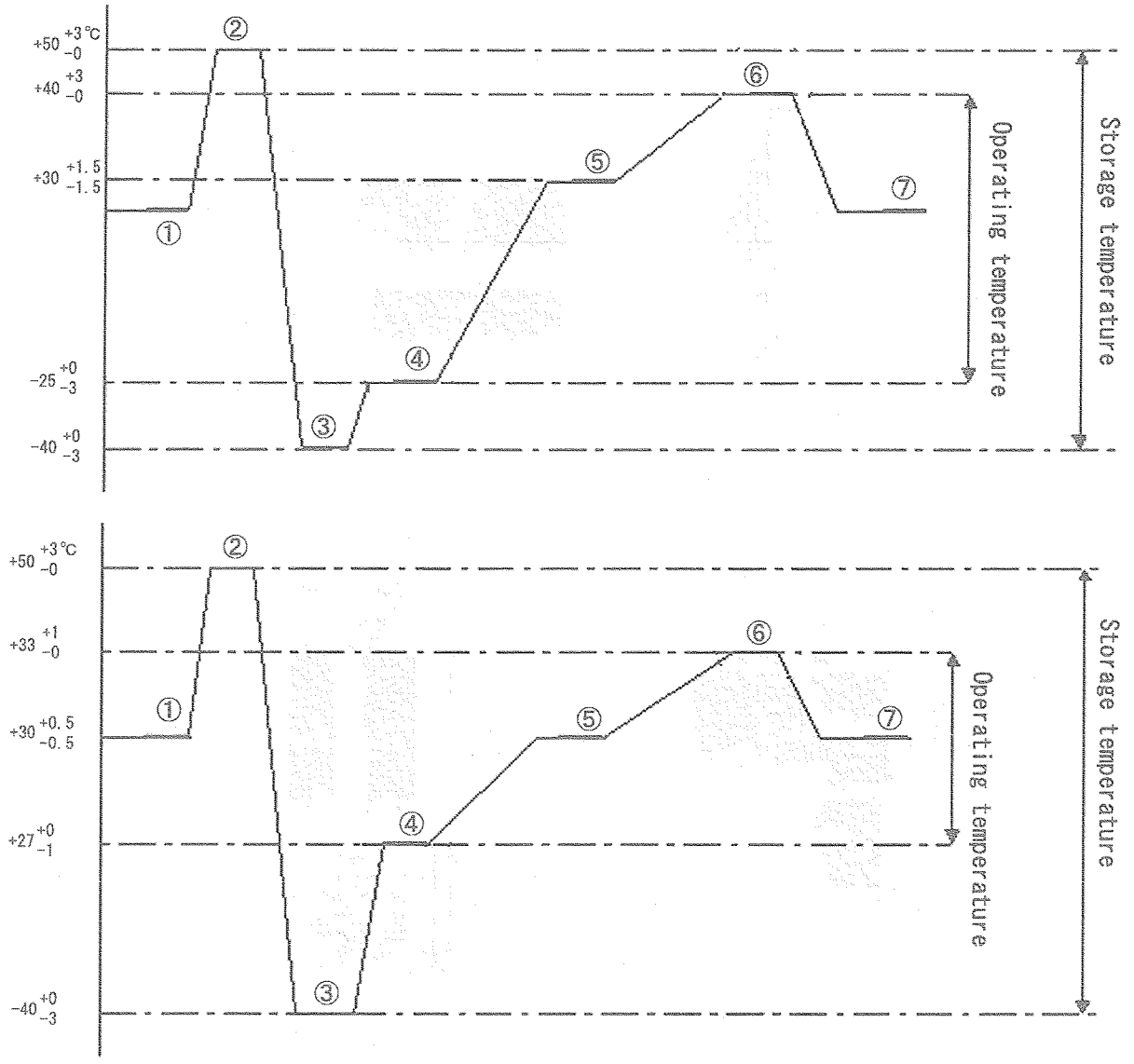

Figure 4-28 Planned temperature profiles of the LIC electronics (upper) and optics (lower) in the TV test. Imaging operations were performed at ① (room temperature), ④ (cold condition), ⑤ (nominal condition), ⑥ (hot condition), and ⑦ (room temperature). Temperature tolerance of the LIC hardware was verified at ② (high temperature condition) and ③ (low temperature condition), where LIC was turned off.

This document is provided by JAXA.

Table 4-13 The points where thermocouples were attached and the corresponding nodes.

Point of thermocouple attachment		Corresponding node in TMM
Optics	Lens 1	210 OPT
	Lens 2	
	CCD	220 CCD COVER
Electronics	JPEG-PWB	310 JPEG
	SIP-PWB	320 SIP
	DSP-PWB	330 DSP
	ASP1-PWB	340 ASP1
	ASP2-PWB	350 ASP2
	Interface (I/F) 1	302 BASE PLATE
	I/F 2	
	Top plate	301 TOP PLATE

(3) Temperature control of LIC

The temperature was controlled during the TV test using both the heaters on the framework for the lens-system and the heaters on the mount. The heaters on the IR panels were used to fine-tune the temperature. The temperature control using the heaters on the framework of the lens-system simulated control by the HCE. The heat loss was mainly via radiation from the surface of the optics. The heat loss from the framework was negligibly small, because the MLI and IR panels surrounded the framework. The diameter of the optics is 5.7cm and the IR absorption efficiency of the glass is 0.8. The heat loss from the optical surface is calculated to be about 1 W. The DC power supply for the heater control is 70V/5A (350W max.) and the maximum heat input at the optical framework is 35 W, well exceeding the heat loss from the optics.

The temperature of the LIC body was controlled using the heaters on the mount. The surface area of the mount facing the shroud was 755cm^2 and the IR absorption efficiency was 0.85. The calculated heat loss from the mount at +40℃ was 35W. The power supply for the heaters on the mount was the same as that for the optics. Therefore, the maximum heat available from the two heaters totaled 163W and easily exceeded the heat loss. The maximum heat released by LIC during imaging operation is 9.3 W, whereas the heat loss from the mount at -25℃ is 13.6W. Therefore, we can control the temperature to -25℃ by compensating for 4.3 W using the heaters.

(4) Results of the tests and adjusting the model

The degree of the vacuum was between 5×10^{-6} and 7×10^{-6} Torr. Figure 4-29 shows the temperature profiles measured using the thermocouples. There was no loss of LIC functions or increase in power consumption. The LIC operation at -25, +30, and 40℃ was normal. The heat release values of the heaters on the optical framework within the operation temperature range were within the designed value.

This document is provided by JAXA.

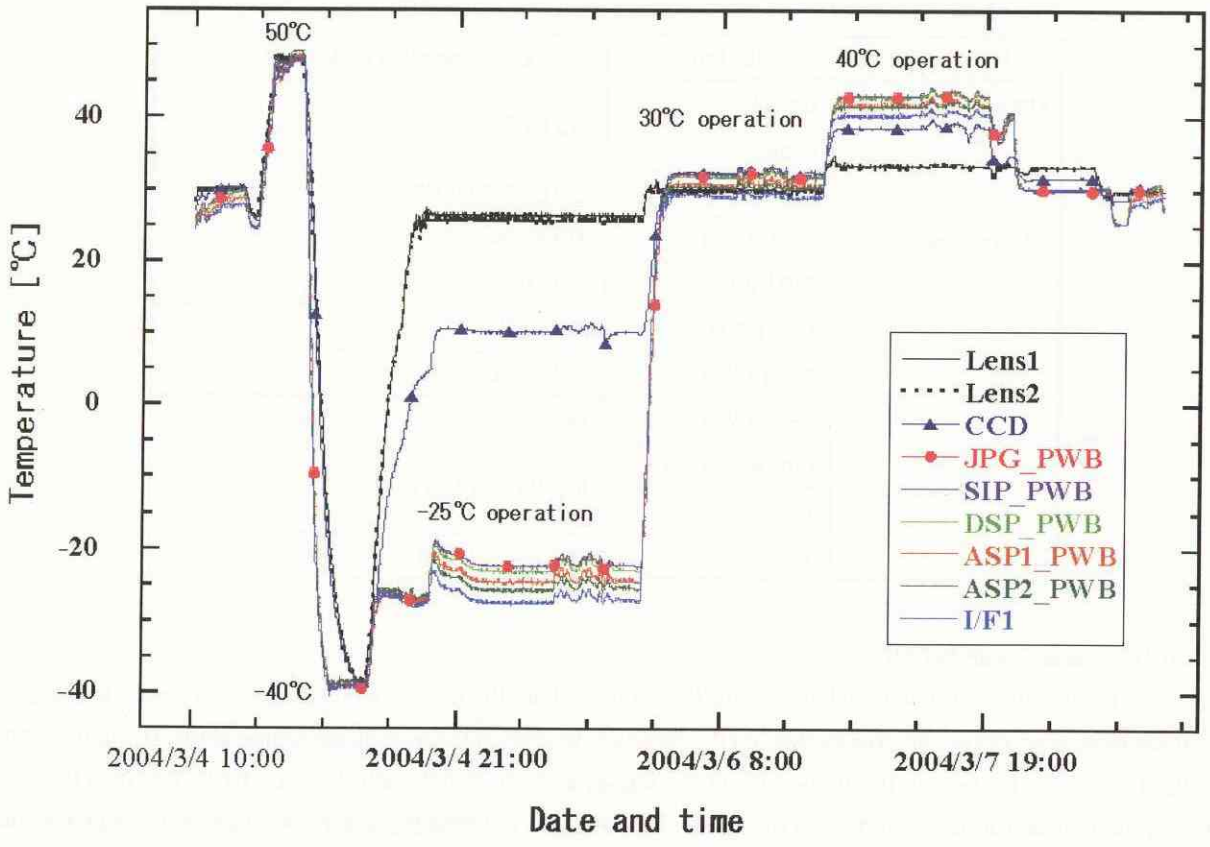

Figure 4-29 Temperature profile of the LIC components at the TV test.

The TMM was evaluated based on the thermocouple temperature data, the power consumption of the LIC electronics, and the input heat from the heaters at -25, +30, and 40℃. Figure 4-30 compares the measured and predicted values. The discrepancy in temperature is within 5℃ for the points in the electronics, whereas the predicted temperatures were much larger than the measured values for the points in the CCD-ASSY at -25℃. The CCD-ASSY was much more isolated in the model. Thermal leakage is expected between the CCD cover and the electronics, judging from the fact that the measured temperature of the CCD was lower than the optical system. Accordingly, heat conduction through the harness between the cover and the electronics was added to the model and we tuned the value of the conductivity of the heat insulation between the optics and electronics. By adopting the conductivity of 2.2 times larger than the designed value for the thermal insulation material, the difference between the measured values and model predictions at almost all nodes fell within 5℃. Consequently, the new adjusted model will be used for the thermal analysis of the total orbiter system and the integrated TV test. The results with the new model are also shown in Figure 4-30.

This document is provided by JAXA.

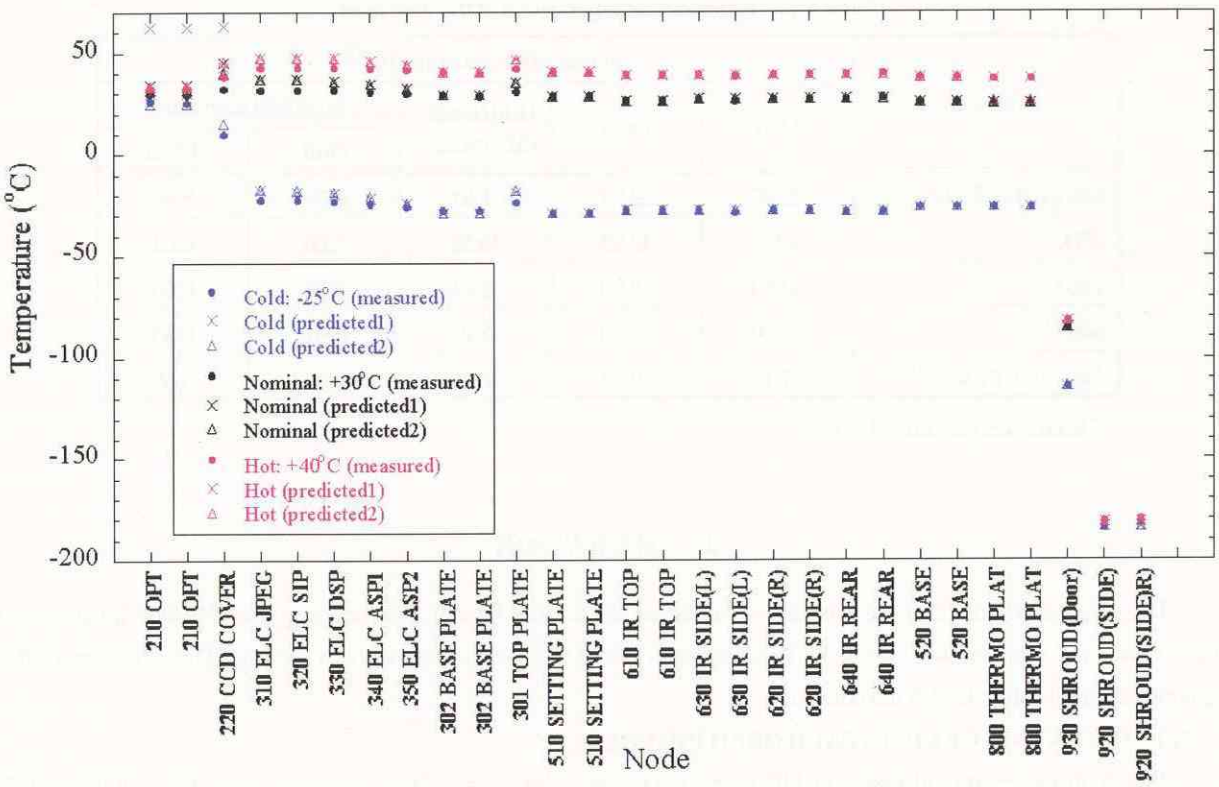

Figure 4-30 Comparison of the measured temperatures and predicted values. SETTING PLATE is the node name for the mount of LIC in Fig. 4-27. The "predicted1" shows the results of the previous model and the "predicted2" shows those of the adjusted model.

(5) Temperature dependence of the LIC performance

Table 4-14 shows the dark level and odd/even difference for each temperature condition. The offset level has a large temperature dependence. According to the predicted flight temperature in the lunar orbiting phase, the expected odd-even difference is 3-5 LSB. However, when the LIC components are integrated in the orbiter, the electrical ground state and stability of the power supply may change. Calibration data for the odd-even difference will be collected by dark images taken during through the integrated TV test and in flight.

(6) Optical performance after the TV test

The optical performance after the TV test was found to be the same as that beforehand, and was within the measurement error (Tables 4-3 and 4-6): there was no change in the performance after exposure to ultrahigh vacuum and high and low temperature.

This document is provided by JAXA.

Table 4-14 Temperature dependence of the dark level

Mode	Dark offset level (LSB) *1)				
	Odd	Even	Odd/Even difference	Standard deviation	
				Odd	Even
Before the TV test *1)	22.87	29.27	6.40	0.75	0.66
-25℃	0.00	40.93	40.93	0.00	0.64
+30℃	23.60	28.46	4.86	0.78	0.66
+40℃	25.70	28.70	3.0	0.61	0.56
After the TV test *1)	21.15	30.34	9.19	0.66	0.59

*1) Room temperature, 1 atm.

5. OPERATION

This chapter summarizes the overview of operation of LIC after launch. Two imaging mode, default imaging and target imaging, and the way to upload imaging parameters for each of them are described. The overview of the ground support system is also introduced.

5. 1. OPERATION OF LIC IN EACH ORBITING PHASE

The main observational phase of LIC is the data-relay orbit at an altitude ranging from 200 to 300 km. LIC consecutively takes the lunar surface images and dark images for calibrations. LIC is also planned to image the Moon and the Earth in the trans-lunar orbit prior to entering into this data-relay orbit for calibration. Moreover, LIC may take high-resolution images of the Moon in the following penetrator separation orbit, where the orbit of the spacecraft is highly eccentric and its altitude becomes very low near the perilune. In the following, the typical operation of each orbiting phase is described along time.

(1) Operation of LIC in the Earth parking orbit

LIC conducts the initial operational test in the Earth parking orbit by imaging the Earth, the Moon, and the dark offset.

(2) Operation of LIC in the Trans-lunar orbit

LIC continues initial operational test in the trans-lunar orbit by taking test images of the Earth and Moon. In this phase, the test is more focused on acquisition of calibration data onboard, such as temperature dependence of dark level and the odd-even differences at each gain mode, because these properties could be changed after the launch.

(3) Operation of LIC in the Penetrator separation orbit

In this phase, there are chances to obtain high-resolution images from perilune at an altitude of 45 km. However, since this is a critical operation phase for the penetrator separation and for checking the initial data link, it requires a close consideration whether LIC operates for imaging in this phase.

(4) Operation of LIC in the Data-relay orbit

LIC images the area near the terminator on the orbit around the moon at an altitude ranging from 200 to 300 km at the low solar altitude. Moderately overlapped consecutive images are taken to avoid gaps between images. Furthermore, the flatfield is obtained by taking lunar images with small incidence angle and by accumulating them.

This document is provided by JAXA.

5. 2. IMAGING MODES

LIC basically starts imaging by TAKE command issued at a particular time. Parameters such as image size, gain, start angle and start pixel, compression factor (see Table 5-1) are all stored in the LIC command buffer in first-in-first-out (FIFO) style for 64 images at the maximum via MODE_SET command issued prior to TAKE. LIC sequentially looks up the imaging parameter at the first entry in the LIC command buffer on imaging, which enables that LIC takes each image with the different parameters. Since LIC is planned to take several tens images every orbit in the data-relay phase, optimal planning of imaging parameter setting is crucial issue in LIC's operation.

There are the two methods to set the imaging parameters.

(1) Transmission of MODE_SET command as a real-time command

Transmit MODE_SET command directly to LIC during the communication path as a real-time command and make the parameters stored in LIC command buffer.

(2) Transmission of MODE_SET command as OGs in OP

The LUNAR-A orbiter is designed to utilize organized command (OG) and operational program (OP) for transmission of commands to simplify its operation. Each OG consists of a series of commands (16 commands at the maximum), and 255 entries of OGs are stored in the spacecraft onboard memory as an OG table. A schedule for conducting OGs is transmitted to the spacecraft as OP, which lists multiple OGs and their time to be issued. Thus we can register MODE_SET command along with imaging parameters in an OG table in advance, and transmit the schedule to issue them as OP prior to the observation. When the time designated in OP comes, corresponding MODE_SET OGs are conducted and the imaging parameters are stored in LIC command buffer automatically.

For simplification of operation, the use of MODE_SET OG in OP is preferred in nominal operation of LIC. However, the number of OGs which can be assigned to LIC's MODE-SET command ranges from 30 to 40[*1)], though such is not sufficient to cover all the possible imaging patterns (e.g., 156). The OG table is rewritable during the mission, however, its update should be kept the least frequent to reduce the risk involved in updating.

Thus we define three operational modes for LIC in terms of the method of MODE_SET command transmission: default imaging (transmission by OGs and OP), target imaging (transmission by real-time commands) and quasi-default imaging (a combination of both methods). One operational unit is defined as the period from the beginning of a communication path until the beginning of the next path. Each operational unit is assigned either one of these three observational modes. The details of each imaging modes are summarized in the following.

A. Default Imaging

In the default imaging, imaging parameters ranging from 30 to 40 are registered as MODE_SET OGs in onboard OG table in advance. LIC images limited areas of the lunar surface by using these parameters via OG and OP. The content of the OG table is updated after a certain period (3-6 months) to image the whole observable lunar area with the optimal imaging parameters. Default imaging parameters and its update schedule are determined to cover as many imaging proposals as possible.

B. Target Imaging

The target imaging copes with imaging proposals that are not covered by the default imaging. In this mode, the imaging parameter is uploaded directly to LIC during the communication path by MODE-SET as a real-time command. The proposals for extremely oblique viewing imaging, the higher latitude imaging outside the nominal imaging area, stereo imaging, and multiple imaging of the specific site at the different viewing condition for photometric study should be conducted in this mode.

This document is provided by JAXA.

C. Quasi-default imaging

Quasi-default imaging is the combination of default imaging and target imaging. However, default imaging should be conducted only ahead of target imaging because of limitation of operation.

---

*1) OGs ranging from 40 to 50 (out of 255 in totals) are assigned to the use of LIC, among which LIC use about 12 OGs for the primal operations such as TAKE. The remaining OGs ranging from 30 to 40 can be assigned to for MODE_SET commands.

5. 3. PARAMETERS FOR DEFAULT IMAGING

In this section, the example of a plan for default imaging is presented.

Suppose LIC images the area close to sub-spacecraft point at the incidence angle larger than 45° to ensure moderately high resolution and high contrast and the least distortion. The image size is fixed to 1024 pixels × 1024 lines for the simplicity (overlap of neighboring images is guaranteed with this size). Most of other imaging parameters can be fixed to one value (see Table 5-1), however, "Gain" and "Start angles" need to be set finely.

Four gains of LIC (Gain0, 1, 2, and 3) are designed to observe both bright and dark areas of the Moon at a wide range of the incidence angle and with a moderately wide dynamic range. Figure 5-1 compares the maximal reflectance observable at each Gain1, 2, and 3, and the reflectance of dark terrain and bright terrain as functions of the (pseudo-) incidence angle. This figure indicates that the optimal gain for observing dark terrain can be always set as Gain3, and for the bright terrain, Gain3 is adequate at the incidence angle larger than 75°, and Gain1 at the incidence angle smaller than 75°. Since the incidence angle of the observation area changes very rapidly during even one orbit (2 hours in time), both gain modes of Gain1 and 3 should be prepared for each of plausible imaging parameter set.

On the other hand, the start angle is set every 0.157 sec (=0.307ms/line×512lines) as time interval along spin, which corresponds to the interval of 3.61 degrees at 3.85rpm. Figure 5-2 shows the optimal start angle to observe the sub-spacecraft point as a function of time. This figure indicates the optimal start angle changes between -25° and 25° (morning on the moon) and 155° and 205° (evening on the moon) every half-year periodically. Allowing the slightly oblique viewing observation in the high latitude, the range of the start angle is defined between either of the ranges between -29° and 29° or 151° and 209°, which leads to 38 patterns for the start angle in total.

Since the same observational condition appears every half-year, we can assign the first half-year to the morning observation and the second half-year to one for the evening observation by rewriting MODE_SET OG of OG tables every half-year. The number of patterns for the start angle is then halved to 19, resulting in 38 imaging parameter set along with 2 for gain in total, which satisfies limitation of the number of OGs allocated for MODE_SET OG.

This document is provided by JAXA.

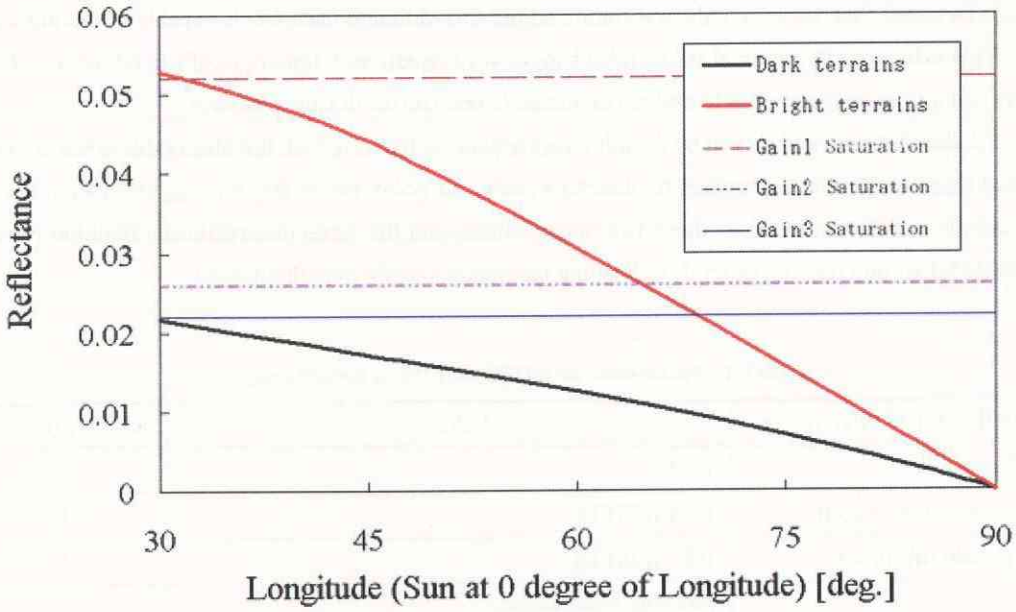

Figure 5-1 Comparison of the reflectance of the dark and bright terrains at the equator with the maximal reflectance observable at each Gain 1, 2, and 3. The reflectance of both terrains is shown as a function of the angle between the orbital plane and the sub-solar point, which corresponds with the incidence angle on the equator. The sensitivity of LIC is based on the designed value. The reflectance values are based on the parameters presented by a previous study (Helfenstein and Veveraka 1987).

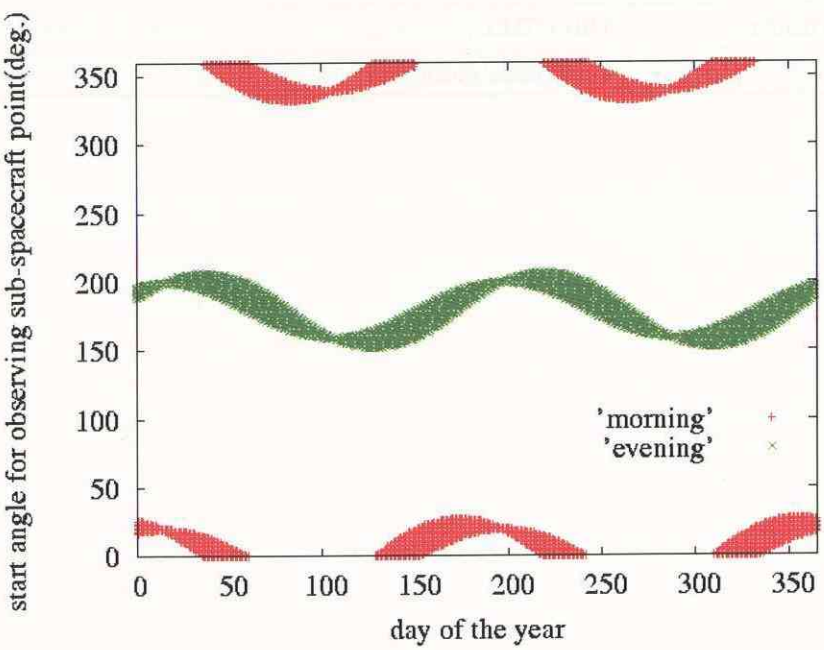

Figure 5-2. Azimuth angle for observing a sub-spacecraft point as a function of time. Red and green plots represent the observation in the morning and the evening, respectively.

This document is provided by JAXA.

It should be noted that we store only one command per OG although each OG is capable of storing maximal 16 commands. This is because the optimal start angle changes very rapidly with time (typically in 80 sec, i.e., 4-5 spins, at the equator) and it is more convenient to assign one image to one OG for flexible planning.

Figure 5-3 shows the area observed by default imaging plan each quarter. All the observable areas are covered by this plan, and there are four opportunities to observe a particular point, two in the evening and two in the morning. The solar altitude is different between these two opportunities, and the same observational condition repeats every half-year. Table 5-1 summarizes an example of imaging parameter sets for default imaging.

Table 5-1 Parameters for MODE_SET OG of default imaging

MODE_SET BC Parameter	Values	Number of cases
AMP-gain	1, 3	2
Size in elevation (pixel)	1024 (FIXED)	1
Size in azimuth (line)	1024 (FIXED)	1
Start Angle (°)	Morning observation {0, 1, 2, 3, 4, 5, 6, 7, 8, 9, 90, 91, 92, 93, 94, 95, 96, 97, 98, 99}×3.61°	19 for each (exchanged every half-year)
	Evening Observation {41, 42, 43, 44, 45, 46, 47, 48, 49, 50, 51, 52, 53, 54, 55, 56, 57, 58, 59} ×3.61°	
Start Pixel	768	1
Scale Factor	TBD (FIXED)	1
Quantization matrix	TBD (FIXED)	1
Compression	Compressed image only	1

This document is provided by JAXA.

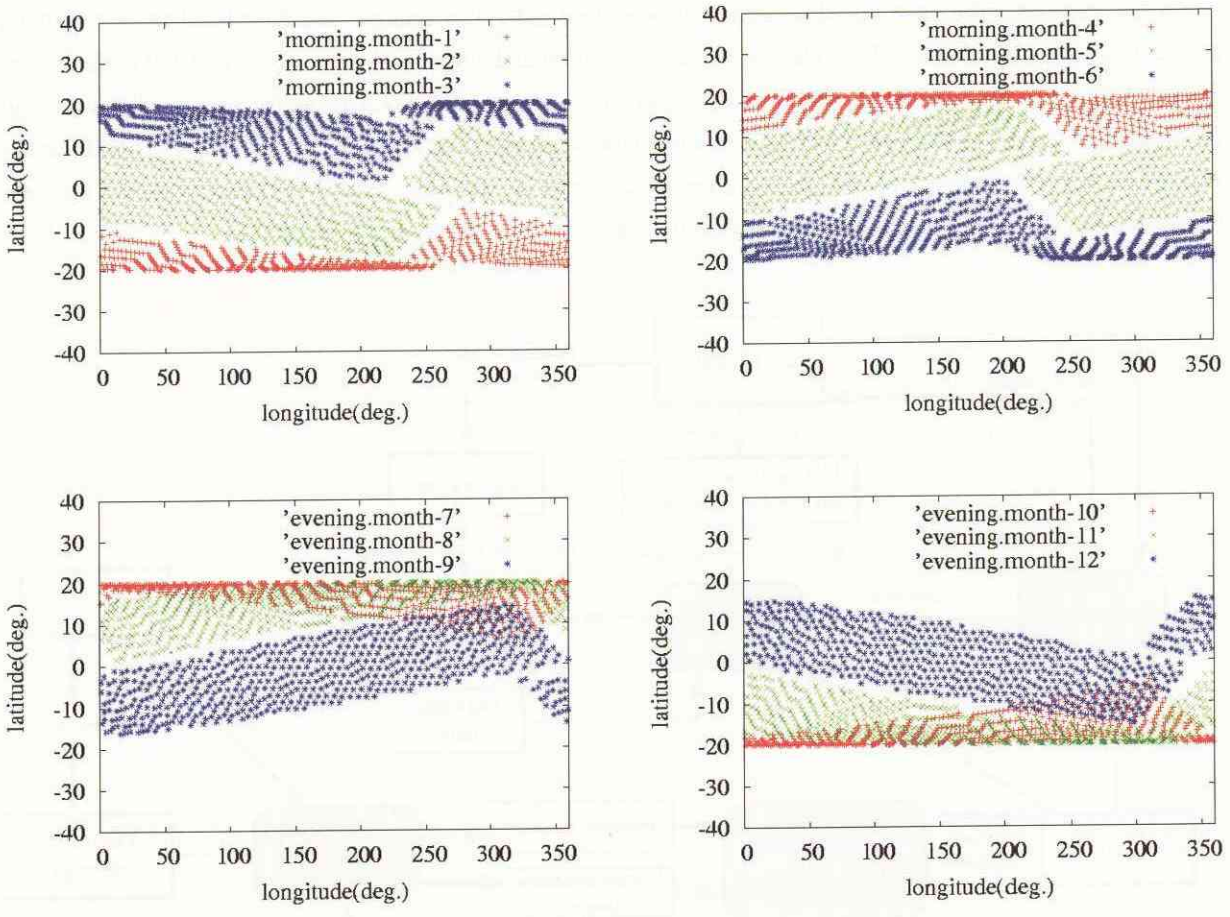

Figure 5-3 An example of imaging areas planned by default imaging. Each plot represent the sub-spacecraft point imaged every three spins and every twelve revolutions. The angle between the orbital plane and the solar direction ranges from 45 to 90°, which corresponds to the incidence angle roughly larger than 45 degrees.

5. 4. LIC GROUND SYSTEM

LIC ground system consists of the following software: LIC Long-term operational plan (LICLOP), LIC short-term operational plan (LICOP), LICTIME, AUTODECO, LICQL and LICIMAGE. The function of each software is described in the following and summarized in Table 5-2. The data flow diagram of LIC ground system is schematically shown in Figure 5-4.

LICLOP assists the long-term operational planning for a whole mission period interactively with graphical interface. LICOP extracts a short-term imaging plan (e.g. weekly) ahead of the planned imaging date (e.g., one week before) and converts the plan into a sequence of commands (MODE_SET and TAKE, as either of OP and OG or real-time commands), and then, it creates Operation Request Language (ORL) files. Intelligent Satellite Control System (ISACS) then checks the consistency and errors of the ORL file and merges it with the requests from the other instruments. Finally the commands are transmitted from the control center to the orbiter.

During and after the operation, LICQL depackets data from either real-time telemetry or from reproduced one from the data recorder (LDP) and browses HK data of LIC and the other instruments related to LIC (e.g., LDP). On depacketing, images (PGM or JPEG) and picture headers are created. AUTODECO is used to decode JPEG compressed images into PGM images after the operation.

This document is provided by JAXA.

A few days after the operation, LICIMAGE creates the level-0 data (images and their headers) determining precise time using LICTIME and the planned values of the orbit and attitude. These data are updated to the higher version data every time the orbit/attitude data are determined or updated. LICIMAGE applies radiometric and geometric corrections to the level-0 data and creates higher-level data. LICTIME is used to convert Time Indicator (TI), time count onboard, to UTC with the accuracy of 0.2 sec on the data-relay orbit, which guarantees the accuracy of spin angle of 0.1° at 3.85 rpm that is comparable to the accuracy of determined attitude of 0.1°.

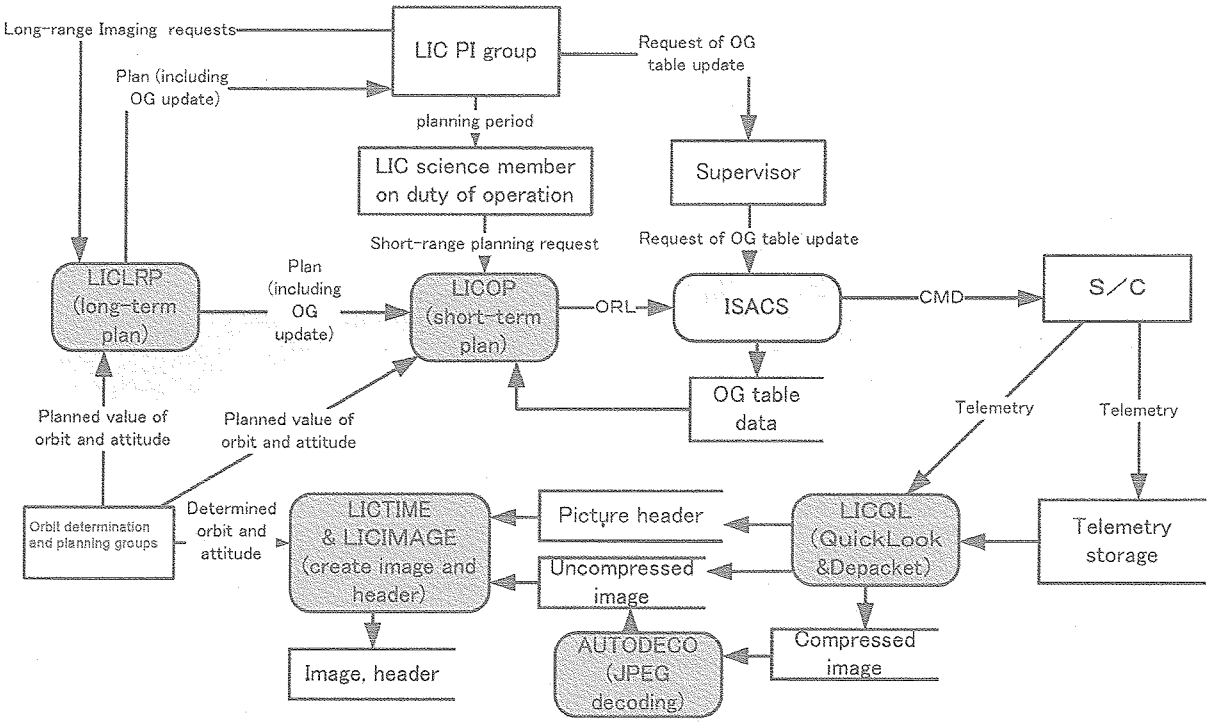

Figure 5-4 The data flow diagram of LIC ground system.

This document is provided by JAXA.

Table 5-2 Summary of software and the function of LIC ground system

Software	Function	Detail of function
LICLOP	Long-term imaging plan	Interactively preview imaging area on the lunar map for imaging planning for scientists.
LICOP	Imaging area visualization	Preview the plausible imaging area on the lunar image.
	A short-range imaging planning	Generate weekly imaging plan by specifying the time or by the area to observe. List all the possible imaging period within the designated period.
	ORL file generation	Generate ORL files from the short-term imaging planning.
	BC generation support	Create the MODE_SET BC command from imaging parameters specified on the screen to assist planning of target imaging.
LICQL	Quick look of telemetry related to LIC	Receive either of in real-time telemetry or one reproduced from the storage, browse HK of LIC and the instruments related to LIC.
	Depacketing of data	Create an image file (PGM and/or JPEG and its picture header by depacketing telemetry data.
AUTODECO	Uncompress JPEG images	Decode a JPEG image into a PGM image.
LICIMAGE	Header addition	Add imaging geometry and other information as header.
	Radiometric calibration	Perform flatfielding.
	Geometric calibration	Project the image onto either of Mercator or sinusoidal map coordinates.
LICTIME	Determination of time in UTC	Convert TI counter(onboard time count) into UTC, by correcting hardware and transmission delays and by calibrating temperature dependence of X'tal oscillator.

Implementation of underlined items has not yet been completed.

6. SUMMARY

LIC is a small, compact and lightweight camera, which consequently constraints its hardware performance and operation. First, the signal from odd and even pixels of the CCD is read separately and then compressed using an irreversible algorithm. Accordingly, the compression error became the dominant error after the usual electrical noise was reduced. The adjustment of the dark levels of the odd and even pixels within an appropriate range at the operating temperature during the lunar orbiting phase was a significant issue during development of the camera system. Second, since the camera uses the spin motion of the orbiter to capture two-dimensional images, we faced a challenge of how to obtain two-dimensional images in the ground tests in a simpler way. Third, LIC has no hood owing to weight limit. The solar paddle will block the direct sunlight to the camera, but the possibility of stray light originating from the light reflected from the lunar surface was not considered in the optical design of the LIC. Therefore, we conducted a test to make a rough estimate of the magnitude of the possible stray light from the lunar surface outside the FOV of LIC.

The nominal downlink bit-rate during the lunar orbiting phase will be 8Kbit/s and the total storage capacity of the LDP is 10 Mbytes, while LIC can use the part of it. An optimal allocation of the imaging plan is highly required and we need to plan the imaging for the entire mission phase roughly and then in more detail one week ahead of the imaging.

This document is provided by JAXA.

Software supporting for the imaging planning was developed for this purpose.

LIC will provide thousands of monochromatic images of the lunar surface with a spatial resolution of about 25m/pixel. The unique observation condition resulting from the large phase angle of LIC will give valuable information on the detailed topography of the lunar surface.

ACKNOWLEDGMENTS

We are grateful to H. Mizutani for his continuous support and encouragement for the LIC project as the leading scientist of the LUNAR-A mission. If it were not for his unflagging enthusiasm and philosophical advice, the task of the LIC team would have been much more difficult. The authors would like to give special thanks to A. Fujimura and S. Tanaka of ISAS for their strong support and valuable comments. We would also acknowledge technical comments and management of T. Nakajima, H. Saito, K. Higuchi, and A. Ohnishi. We greatly appreciated I. Nakatani's efforts in managing the international collaboration with CNES for the supply of the JPEG-ICM chip. The LIC instrument was manufactured by NEC Toshiba Space Systems (NTSpace). J. Ishida and technical staffs at the NTSpace are greatly acknowledged for their dedicated work during the manufacture of the instrument and the ground tests. Finally, we would like to express our thanks to all the members of the former Comparative Planetology group of ISAS for their assistance and cooperation for the LIC project.

REFERENCES

Baldwin, R. B.: The measure of the moon, Univ. Chicago Press, Chicago, 488p, 1963.

Chabot, N. L., G. V. Hoppa and R. G. Strom: Analysis of lunar lineaments; far side and polar mapping, *Icarus*, **147**, 301-308, 2000.

Freed, A. M., H. J. Melosh and S. C. Solomon: Tectonics of mascon loading: resolution of the strike-slip faulting paradox, *J. Geophys. Res.*, **106**, 20603-20620, 2001.

Golombek, M. P.: Structural analysis of lunar grabens and the shallow crustal structure of the Moon, *J. Geophys. Res.*, **84**, 4657-4666, 1979.

Hapke, B.: Bidirectional reflectance spectroscopy: 1. theory, *J. Geophys. Res.* **86**, B4, 3039-3054, 1981.

Hapke, B.: Bidirectional reflectance spectroscopy: 3. correction for macroscopic roughness, *Icarus*, **59**, 41-59, 1984.

Hapke, B. and E. Wells: Bidirectional reflectance spectroscopy: 2. experiments and observations, *J. Geophys. Res.*, **86** B4, 3055-3060, 1981.

Head, J. W.: Morphology and structure of the Taurus-Littrow highlands (Apollo 17): evidence for their origin and evolution, *The Moon*, **9**, 355-393, 1974.

Helfenstein, P. and J. Veverka: Photometric properties of lunar terrains derived from Hapke's equation, *Icarus*, **72**, 342-357, 1987.

Horz, F., R. Grieve, G. Heiken, P. Spudis and A. Binder: Lunar surface processes, in *Lunar sourcebook*, edited by G. H. Heiken, D. T. Vaniman and B. M. French, Cambridge Univ. Press, New York, 61-120, 1991.

Howard, K. A. and W. R. Muehlberger: Lunar thrust faults in the Taurus-Littrow region, *NASA Spec. Publ.*, **330**, 31-22 to 31-21, 1973.

Kirk, R. L. and D. J. Stevenson: The competition between thermal contraction and differentiation in the stress history of the Moon, *J. Geophys. Res.*, **94**, 12133-12144, 1989.

Kreslavsky, M. A., Y. G. Shkuratov, Y. I. Velikodsky, V. G. Kaydash, and D. G. Stankevich, and C. M. Pieters: Photometric properties of the lunar surface derived from Clementine observations, *J. Geophys. Res.*, **105**, E8, 20281-20295, 2000.

Lucchitta, B. K.: Mare ridges and related highland scarps-result of vertical tectonism? *Proc. Lunar Sci. Conf. 7th*, 2761-2782, 1976.

This document is provided by JAXA.

Lucchitta, B. K. and J. A. Watkins: Age of graben systems on the moon, *Proc. Lunar Sci. Conf. 9th*, 3459-3472, 1976.

Maxwell, T. A., F. El-Baz and S. H. Ward: Distribution, morphology and origin of ridges and arches in Mare Selenitatis, *Bull. Geol. Soc. Am.*, **86**, 1273-1278, 1976.

McEwen, A. S.: Photometric functions for photoclinometry and other applications, *Icarus*, **92**, 298-311, 1991.

McGill, G. E.: Attitudes of fractures bounding straight and arcuate lunar rilles, *Icarus*, **14**, 53-58, 1971.

Melosh, H. J.: The tectonics of mascon loading, *Proc. Lunar Planet. Sci. Conf. 9th*, 3513-3525, 1978.

Melosh, H. J.: Tectonic patterns on a tidally distorted planet, *Icarus*, **43**, 334-337, 1980.

Ninomiya, K., T. Hashimoto, A. M. Nakamura, T. Mukai, M. Nakamura, M. Ogasawara, N. Yoshizawa, J. Ishida, Y. Mizushima, H. Hosoda, and M. Takano., Mars imaging camera (MIC) on board PLANET-B, Third IAA International Conference on Low-Cost Planetary Missions, Pasadena, U.S.A, 1998.4, *Acta Astronimica*, **45**, pp. 597-604, 1999.

Nozette, S. et al.: The Clementine mission to the Moon; scientific overview, *Science*, **266**, 1835-1839, 1994.

Pinet, P., P. Cerroni, J.-L. Josset, S. Beauvivre, S. Chevrel, K. Muinonen, Y. Langevin, M, A.Barucci, M. C. De Sanctis, Yu. Shkuratov, V. Shevchenko, P. Plancke, B. A. Hofmann, M. Josset, P. Ehrenfreund, Z. Sodnik, D. Koschny, M. Almeida and B. Foing: The advanced moon micro-imager experiment (AMIE) on SMART-1: Scientific goals and expected results, *Planet. Space Sci.*, **53**, 1309-1318, 2005.

Schubert, G., T. Spohn and R. T. Reynolds: Thermal histories, compositions and internal structures of the moons of the solar system, in *Satellites*, edited by J. A. Burns and M. S. Matthews, Univ. Arizona Press, Tucson, 224-292, 1986.

Schultz, P. H. et al.: Interpreting statistics of small lunar craters, *Proc. Lunar Sci. Conf. 8th*, 3539-3564, 1977.

Sharpton, V. L. and J. W. Head: Stratigraphy and structural evolution of southern Mare Serenitatis: a reinterpretation based on Apollo Lunar Sounder Experiment data, *J. Geophys. Res.*, **87**, 10983-10998, 1988.

Solomon, S. C.: The relationship between crustal tectonics and internal evolution in the Moon and Mercury, *Phys. Earth Planet. Inter.*, **15**, 135-145, 1977.

Solomon, S. C.: On the early thermal state of the Moon, in *Origin of the Moon*, edited by W. K. Hartmann, R. J. Philips, and G. J. Taylor, Lunar and Planetary Institute, Houston, 435-452, 1986.

Solomon, S. C. and J. Chaiken.: Thermal expansion and thermal stress in the Moon and terrestrial planets: clues to early thermal history, *Proc. Lunar Sci. Conf. 7th*, 3229-3243, 1976.

Solomon, S. C. and J. W. Head: Vertical movement in mare basins: relation to mare emplacement, basin tectonics and lunar thermal history, *J. Geophys. Res.*, **84**, 1667-1682, 1979.

Solomon, S. C. and J. W. Head: Lunar mascon basins: lava filling, tectonics, and, evolution of the lithosphere, *Rev. Geophys. Space Phys.*, **18**, 107-141, 1980.

Trask, N. J. and L. C. Rowan: Lunar orbiter photographs-some fundamental observations, *Science* **158**, 1529-1535, 1967.

Vickery, A. M.: Size-velocity distribution of large ejecta fragment, *Icarus* **67**, 224-236, 1986.

Vickery, A. M.: Variation in ejecta size with ejection velocity, *Geophys. Res. Lett.* **14**, 726-729, 1987.

Wijker, J.: Chapter 10 in *Mechanical vibrations in spacecraft design*, Springer-Verlag, Berlin Heidelberg, 2004.

Wilhelms, D. E.: The geologic history of the Moon, *U.S. Geol. Surv. Prof. Pap.* no. **1348**, 302p, 1987.

This document is provided by JAXA.

APPENDIX: RANGES OF INCIDENCE ANGLE, EMISSION ANGLE, AND PHASE ANGLE OF LIC IMAGING

A. 1 RANGE OF PHASE ANGLE (α)

The inclination of the spacecraft orbital plane is 20° and the spacecraft orbits around the Moon every two hours. The spin axis of spacecraft is mostly parallel to the direction of Sun (a small deviation is allowed), and the viewing direction at the center of the LIC's FOV is fixed to be perpendicular to the spin axis of the spacecraft. A solar angle s is defined as an angle between the direction of the sun and the spacecraft's spin axis as shown in Figure A-1. For simplification, let us assume the spin axis is parallel to the equatorial plane of the Moon, and LIC observes along this plane. Under this situation, phase angle at the center of FOV ranges from $(90° - s)$ to $(90° + s)$ in one revolution around the Moon. LIC covers ca. $\pm 7.3°$ from the center of the FOV in this plane. Therefore, the minimum and maximum phase angles within the FOV at this revolution are $(82.7° - s)$ and $(97.3° + s)$, respectively. The solar angle s is controlled to be smaller than 30°, for the solar battery requirement. As a result, the minimum and maximum phase angles for overall observation period are 52.7° and 127.3°, respectively.

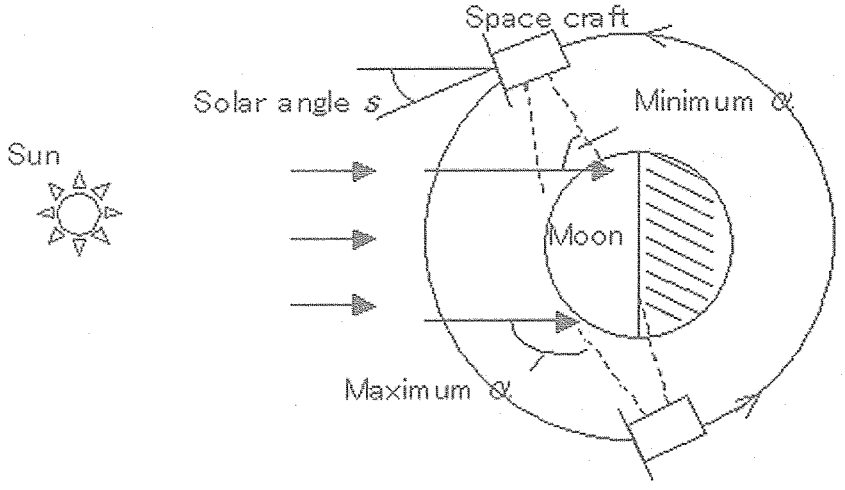

Figure A-1 The maximum and minimum phase angles. This cartoon is a view from polar direction of the Moon.

A.2 RANGE OF INCIDENCE ANGLE (i) AND EMISSION ANGLE (e)

The incidence angle i for a lunar surface element is defined as an angle between the normal vector of the lunar surface and the direction of the sun. The emission angle e is defined as an angle between the normal vector and the direction of LIC as shown in Figure A-2. If we allow any observable area between the terminator (e.g. observed from 1 and 4 in Figure A-2) and the horizon (e.g. observed from 2 and 3 in Figure A-2) for photometric studies, e ranges from 0° to 90°, and i ranges from 0° to 90°. The values of i, e, and α are interdependent so that α becomes the angle between the incident vector and the emission vector ($i + e \geq \alpha$).

Spatial resolution of a LIC image of lunar surface is ~25m/pixel at the spacecraft's altitude of 250km. At such fine spatial resolution, the normal vector varies from place to place on the Moon, depending not only on the global shape of the Moon but also on the local topography as illustrated in Figure A-3.

This document is provided by JAXA.

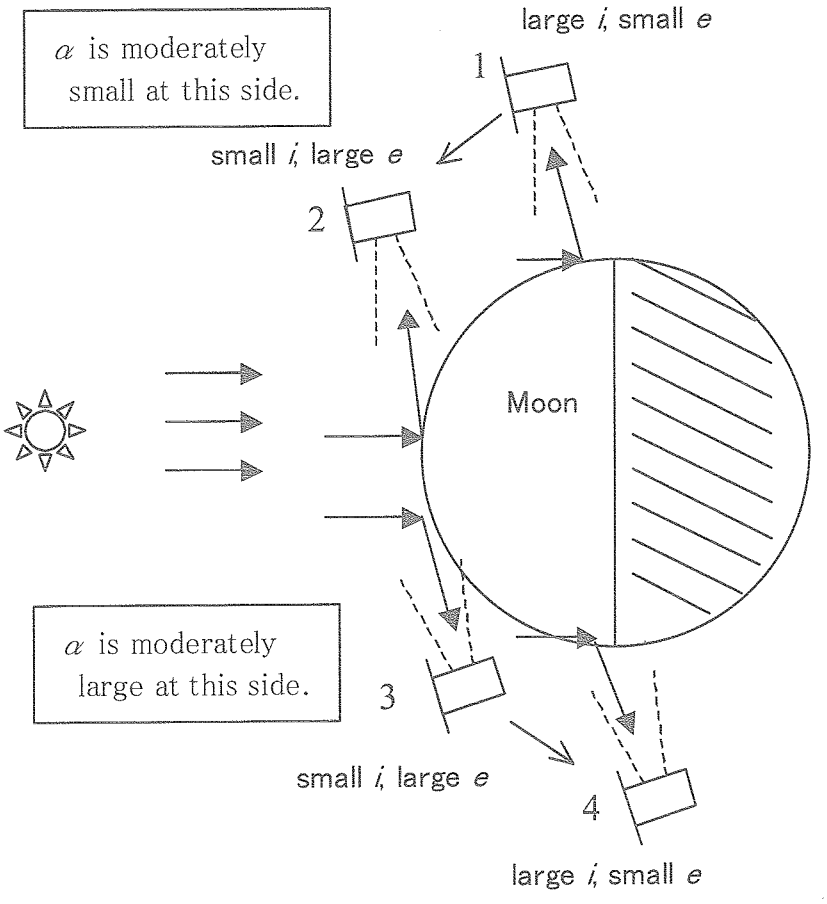

Figure A-2 Relations between the incidence angle *i* and the emission angle *e*. This cartoon is a view from the polar direction of the Moon.

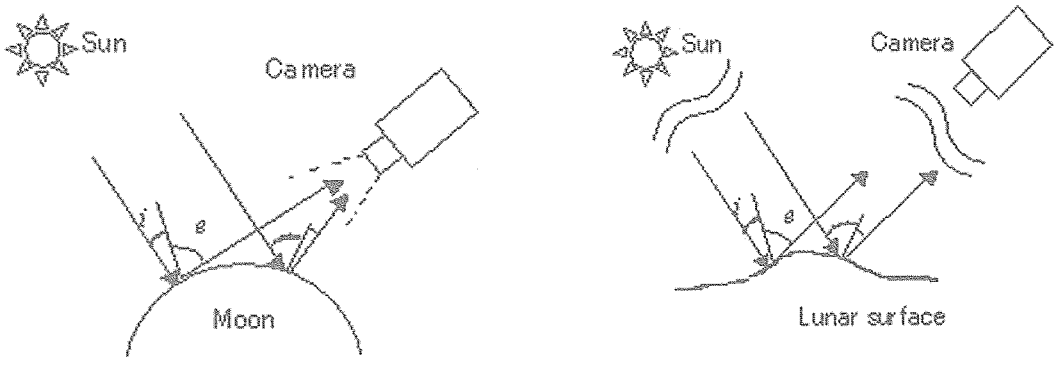

Figure A-3 (Left) Geometry at large scale. Incidence and emission angles are changed by global curvature of the lunar surface. (Right) Undulation of the lunar surface also makes variation of incidence and emission angles.

This document is provided by JAXA.

This document is provided by JAXA.

JAXA Research and Development Report
(JAXA-RR-04-046E)

Date of Issue : March 31, 2005

Edited and Published by :
Japan Aerospace Exploration Agency
7-44-1 Jindaiji-higashimachi, Chofu-shi,
Tokyo 182-8522 Japan

Printed by :
FUJIPLANS Co., Ltd.
3-8-2 Toukai, Ota-ku, Tokyo 143-0001 Japan

© 2005 JAXA, All Right Reserved

Inquires about copyright and reproduction should be addressed to the Aerospace Information Archive Center, Information Systems Department JAXA. 2-1-1 Sengen, Tsukuba-shi, Ibaraki 305-8505 Japan.

Printed on Recycled Paper
This document is provided by JAXA.

Japan Aerospace Exploration Agency

This document is provided by JAXA.